

## Supplementary Information

For

### Engineering charge transfer by tethering halogens onto covalent organic framework for photocatalytic sacrificial hydrogen evolution

Fangpei Ma,<sup>‡a</sup> Xiao Chi,<sup>‡b</sup> Ying Wen,<sup>a</sup> Qihong Yue,<sup>a</sup> Tao Chen,<sup>a</sup> Xiaojiang Yu,<sup>c</sup> Xiaoling Liu,<sup>a</sup> Yu Zhou<sup>\*a</sup> and Jun Wang<sup>\*a</sup>

<sup>a</sup> State Key Laboratory of Materials-Oriented Chemical Engineering, College of Chemical Engineering, Nanjing Tech University, Nanjing, 211816, China

<sup>b</sup> Department of Physics, National University of Singapore, 117576, Singapore

<sup>c</sup> Singapore Synchrotron Light Source, National University of Singapore, 5 Research Link, 117603, Singapore

‡ These authors contributed equally: Fangpei Ma and Xiao Chi.

### Corresponding Authors

Email: njutzhouyu@njtech.edu.cn (Y. Zhou); junwang@njtech.edu.cn (J. Wang)

## General experimental methods

### Instrumentation

Powder X-ray diffraction (PXRD) patterns were recorded on a Smart Lab diffractometer (Rigaku Corporation) with a Cu rotating-anode source at 9 kW with the wavelengths of 1.5406 Å and 1.5444 Å. The voltage was 40 kV and the tube current were 40 mA. The scanning angle ( $2\theta$ ) range was from  $2^\circ$  to  $30^\circ$ , with scanning speed of  $5^\circ/\text{min}$  and the step size of  $0.02^\circ$ . The morphology of COFs was investigated using a field emission scanning electron microscope (FE-SEM; Hitachi S-4800) with the powder sample dispersed on the conductive adhesive. Transmission electron microscopy (TEM) images were obtained on a JEOL (JEM-2100F, 200 kV) field-emission transmission electron microscope. The point resolution was  $\leq 0.23 \text{ nm}$  and the line resolution was  $\leq 0.14 \text{ nm}$ . The powder sample was dispersed in ethanol and then dropped on 300-mesh carbon-coated copper grid. A BELSORP-Max analyzer was exploited in the collection of nitrogen ( $N_2$ ) sorption isotherms at 77 K for the analysis of surface areas and porosity. The Brunauer-Emmett-Teller (BET) method was employed to analyze the nitrogen desorption data to obtain the average pore diameter of the sample by using the equation of  $D=4V_p/S$  ( $S$ : specific surface area,  $V_p$ : pore volume, and  $D$ : pore diameter). The pore size distribution profiles were calculated by using the non-local density functional theory (NLDFT) with the cylindrical pore model. The pore size dispersion curve revealed the position of the most probable pore size. X-ray photoelectron spectroscopy (XPS) spectra were recorded on an X-ray photoelectron spectrometer (AXIS Supra) outfit with Al  $K\alpha$  radiation. The binding energy was calibrated through C1s at 284.8 eV. The scanning range was from 0 eV to 1500 eV and the step size was 0.2 eV. Fourier transform infrared spectra (FTIR) of raw materials and COFs were collected with an Agilent Cary 660 instrument by using a Deuterated Triglycine Sulfate (DTGS) detector. The scanning range of the mid-infrared region is  $4000\text{-}400 \text{ cm}^{-1}$ . The resolution of the FTIR instrument was  $1\text{-}4 \text{ cm}^{-1}$ , and the number of scans was 64 times. The aperture size was  $1 \text{ cm}^2$ . During the measurement, 1 mg of the sample was thoroughly ground and mixed evenly with 150 mg of dry potassium bromide (KBr) powder in an agate mortar. Then, the mixture was placed in a tablet press and pressed into a transparent thin sheet under a 10 MPa pressure for the following test. UV-vis spectra were collected with a Shimadzu UV 2600 spectrometer with  $\text{BaSO}_4$  as the internal standard. External single detector was adopted, with a slit width of 5.0 nm. An RF-5301/PC

spectrofluorophotometer (Shimadzu, Japan) was involved in the collection of photoluminescence (PL) emission spectra at room temperature. Time-resolved PL decay spectra were recorded in an FLS1000 fluorescence lifetime spectrophotometer (Edinburgh Instruments, UK). Elemental analyses were carried out on a Vario EL cube CHN elemental analyzer. The combustion temperature was 1000 °C. The carrier gas was helium with a flow rate of 200 mL/min. Thermogravimetric analysis (TGA) was collected with an STA409 instrument using a heating rate of 10 °C min<sup>-1</sup> to 800 °C under a dry N<sub>2</sub> atmosphere. Solid-state <sup>13</sup>C cross-polarization (CP)/magic-angle-spinning (MAS) nuclear magnetic resonance (NMR) spectra were recorded on an AVABCE-III NMR spectrometer (Bruker, Switzerland) with a spinning rate of 6 kHz, a contact time of 2.0 ms, and a recycle delay of 15.0 s. The solid sample was grinded into fine powder and dried under vacuum to remove the water. After that, the sample was carefully filled into a ceramic NMR rotor to be collect the NMR spectra. Water vapor isotherms were determined by a BELSORP-Max analyzer at 298 K. The content of possible residue noble metals (Pd, Pt, and Au) was measured by inductively coupled plasma-mass spectrometry (Agilent 7850).

### **Photoelectrochemical measurements**

Photoelectrochemical properties were conducted by using a CHI 760E electrochemical workstation (Shanghai Chen-hua, China) with a Pt foil as the counter electrode, Ag/AgCl (saturated KCl) as the reference electrode, the FTO glass coated catalyst as the photoelectrode, 0.5 M aqueous Na<sub>2</sub>SO<sub>4</sub> solution as the electrolyte. The slurry was prepared by mixing 5 mg of COF with 440 µL of 10% Nafion ethanol solution. The working electrode was prepared by drop-casting 88 µL of the above slurry on carbon paper (1×1 cm<sup>2</sup>) to cover a 1 cm<sup>2</sup> area and dried completely. For photocurrent measurement, a 300 W Xe lamp (Perfect Light PLSSXE 300) equipped with a 420 nm cut off filter ( $\lambda > 420$  nm) was used as the illumination source. Electrochemical impedance spectroscopy (EIS) was measured at open-circuit voltage with an Alternating Current (AC) amplitude of 5 mV in the frequency range of 0.1 Hz to 100 kHz.

### ***Quasi in-situ* electron paramagnetic resonance**

*Quasi in-situ* electron paramagnetic resonance (ESR) experiments were performed on Bruker EMXmicro spectrometer. Before the ESR measurement, a suspension containing the COF powder

and the solvent ( $\text{H}_2\text{O}/0.1 \text{ M AA solution}/3.5 \text{ wt\% NaCl solution}$ , 1 mg/mL) was added to the quartz tube, and the test temperature was set at 298 K. The ESR signals were collected on a Bruker EMXmicro spectrometer under illumination by using a 300 W Xe lamp as the light source ( $\lambda > 420 \text{ nm}$ ). For comparison, the signal was also collected in the dark.

### **Transient absorption spectroscopy (TAS)**

Transient absorption spectroscopy (TAS) spectra were measured with a Laser Flash photolysis (LFP, Dalian Institute of Chemical Physics) under room temperature. The sample (5 mg) and NaCl solution (5 mL, 3.5 wt%) were mixed and ultra-sonicated for 30 min to give a relatively homogeneous slurry. The slurry (1 mg/mL) was excited at 355 nm pulses from Nd:YAG nanosecond laser system (Nimma900, Beamtech Optronics Co., Ltd.). A pulsed 450W xenon lamp (PL450, Dalian Institute of Chemical Physics) was used as the probe light. The single-wavelength transient absorption kinetics was detected with a photomultiplier tube (R928, Hamamatsu), and the transient curve was recorded by a digital oscilloscope (Tektronix, MDO3052).

### **Soft X-ray absorption spectroscopy experiments**

Soft X-ray absorption spectroscopy (XAS) analysis was performed on the Surface, Interface, and Nanostructure Science (SINS) beamline of the Singapore Synchrotron Light Source, equipped with a Scienta R4000 electron energy analyzer.

### **Computational Methods**

All calculations were generated with the Gaussian 09 program package. All investigated structural models were optimized with B3LYP/def2-SVP level of theory[1,2]. Grimm's empirical D3 dispersion correction with Becke-Johnson damping (D3BJ) was used in these calculations. The effect of water solvation was simulated by using the PCM/SMD solvation model[3]. We evaluated the redox potential of the different molecular fragments representing the COFs relative to  $\text{H}^+/\text{H}_2$  redox potential. The calculation of the ionization potential (IP) and electron affinity (EA) was performed with B3LYP/def2-SVP level of theory. Time-dependent DFT (TD-DFT) was used to evaluate the exciton potentials (i.e., exciton ionization potential ( $\text{IP}^*$ ) and exciton electron affinity ( $\text{EA}^*$ )). Charge distribution over optimized structural models was calculated by B3LYP/Def2-SVP level of theory.

Gibbs free energy change for H\* adsorption ( $\Delta G_{H^*}$ ) was calculated *via* the following equation:

$$\Delta G_{H^*} = \Delta E + ZPE - T\Delta S$$

Where  $ZPE$  is the zero-point energy difference and  $\Delta S$  is the entropy difference between hydrogen adsorption and hydrogen in the gas phase.

Owing to the effects of the catalyst on both  $ZPE$  and  $\Delta S$  being negligible, their values can be directly obtained from references without considering the contribution of the catalyst. Then, the Gibbs free energy change for H\* adsorption can be calculated *via* the following equation:

$$\Delta G_{H^*} = \Delta E + 0.24$$

$$\Delta E = E_{H-cof} - E_{COF} - \frac{1}{2}E_{H_2}$$

Where  $E_{H-COF}$  is the energy of a hydrogen atom adsorbed on the COF surface and  $E_{COF}$  is the energy of COF, and  $E_{H_2}$  is the energy of a hydrogen molecule.

## Results and Discussion

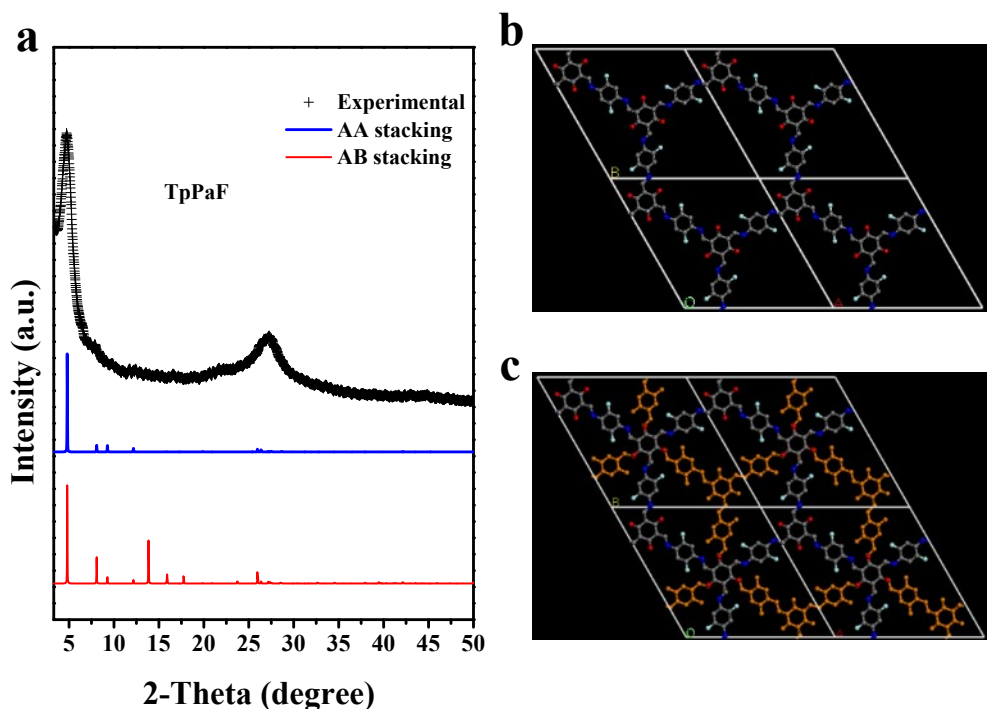


**Fig. S1.** (a) Experimentally observed PXRD patterns (black) of TpPaF and the simulated ones of AA-stacking (blue), AB-stacking (red). (b) Top view of simulated AA stacking mode and (c) AB stacking mode for TpPaF crystal structure.

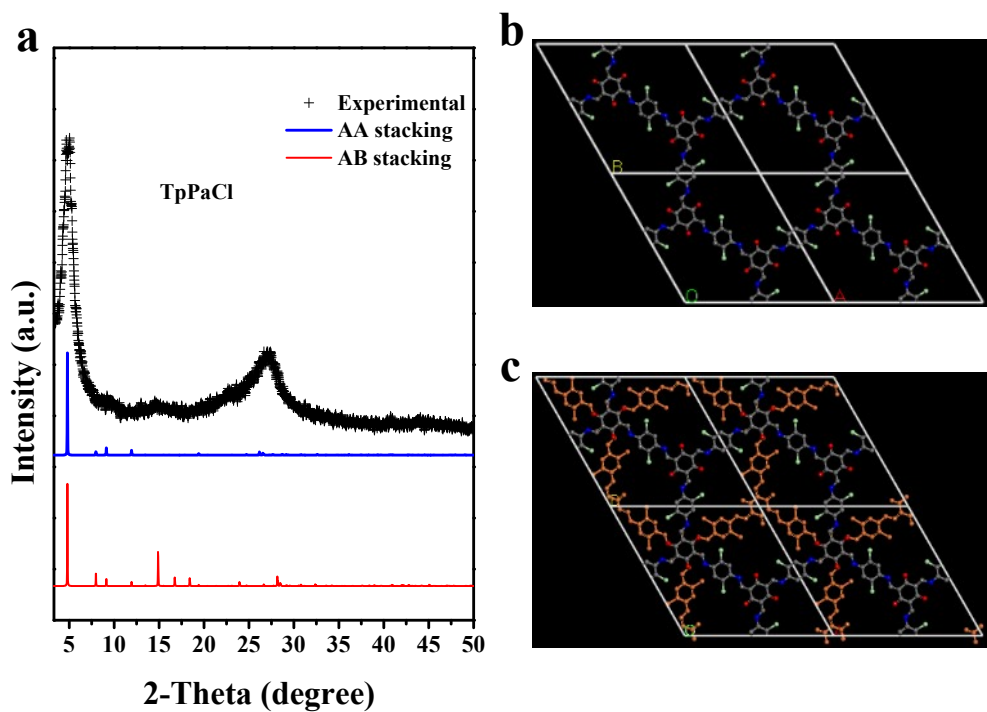


**Fig. S2.** (a) Experimentally observed PXRD patterns (black) of TpPaCl and the simulated ones of AA-stacking (blue), AB-stacking (red). (b) Top view of simulated AA stacking mode and (c) AB stacking mode for TpPaCl crystal structure.

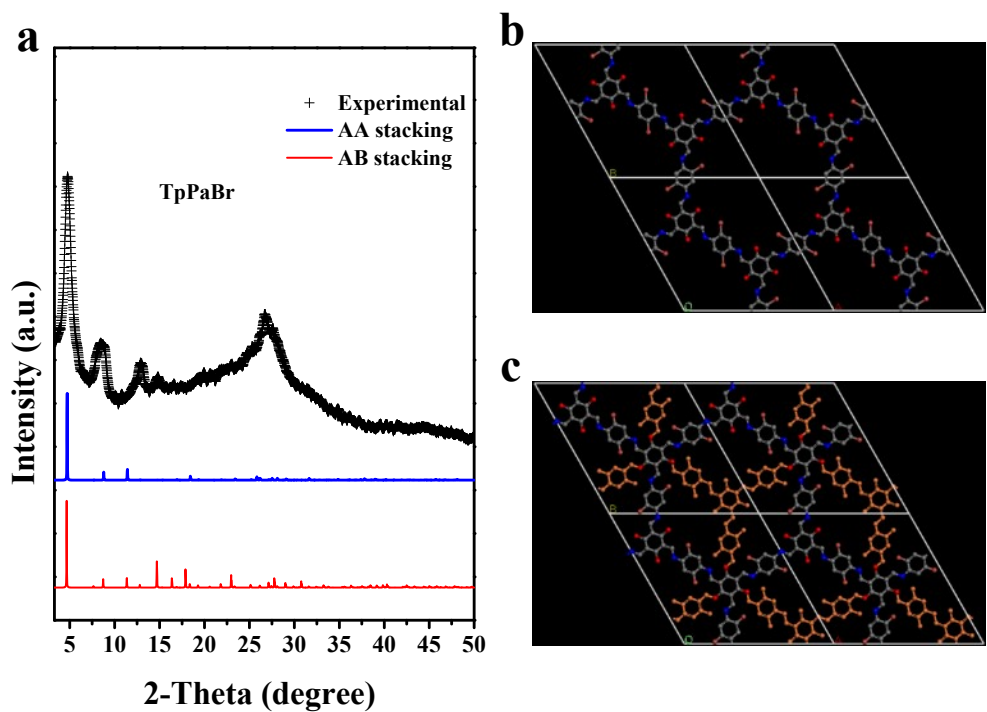


**Fig. S3.** (a) Experimentally observed PXRD patterns (black) of TpPaBr and the simulated ones of AA-stacking (blue), AB-stacking (red). (b) Top view of simulated AA stacking mode and (c) AB stacking mode for TpPaBr crystal structure.

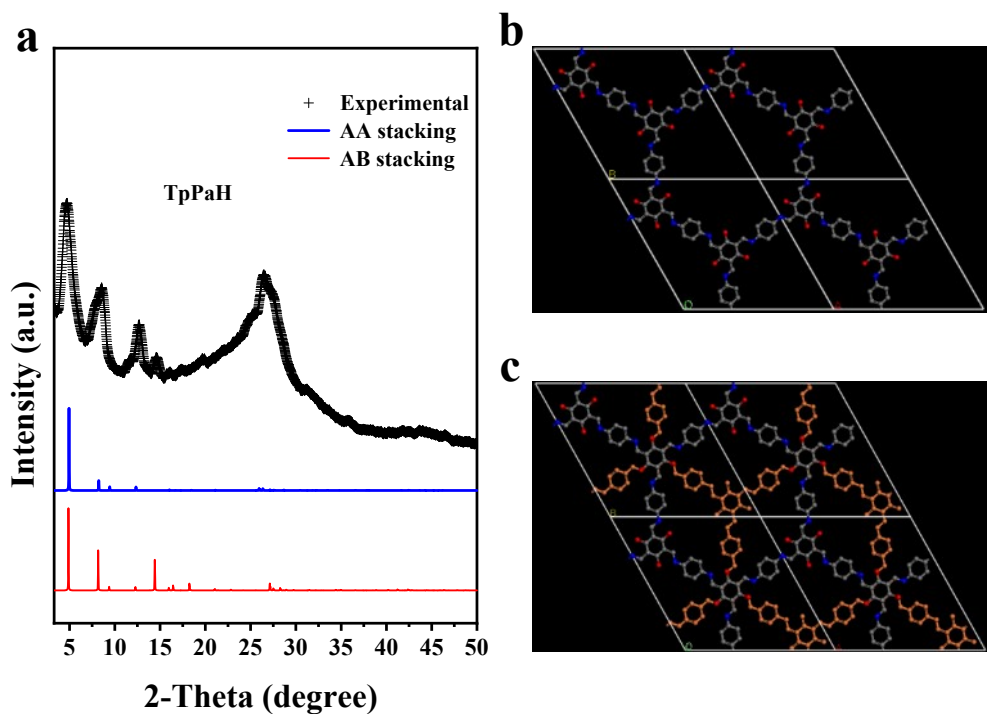


**Fig. S4.** (a) Experimentally observed PXRD patterns (black) of TpPaH and the simulated ones of AA-stacking (blue), AB-stacking (red). (b) Top view of simulated AA stacking mode and (c) AB stacking mode for TpPaH crystal structure.

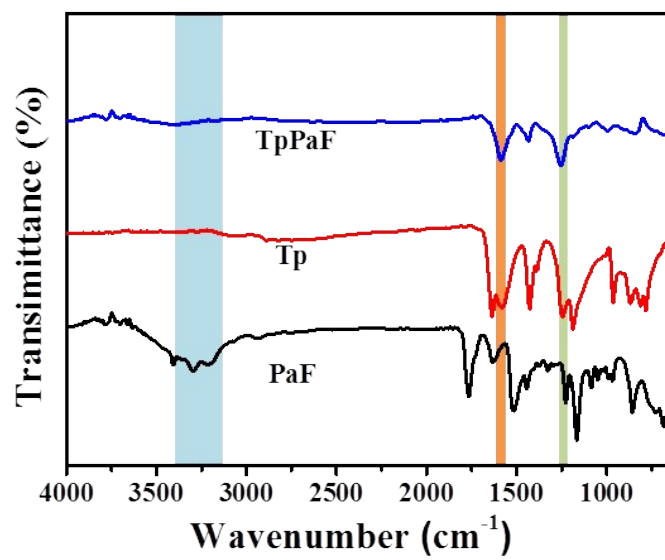


**Fig. S5.** FT-IR spectra of Tp, PaF, and TpPaF.

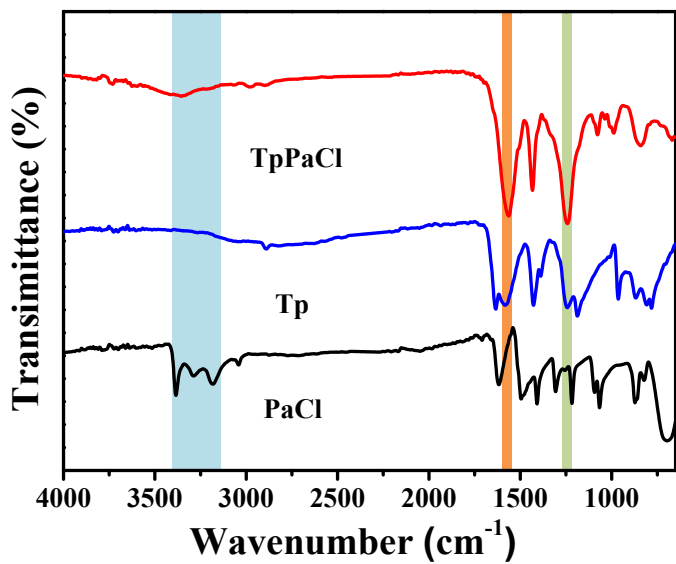


**Fig. S6.** FT-IR spectra of Tp, PaCl, and TpPaCl.

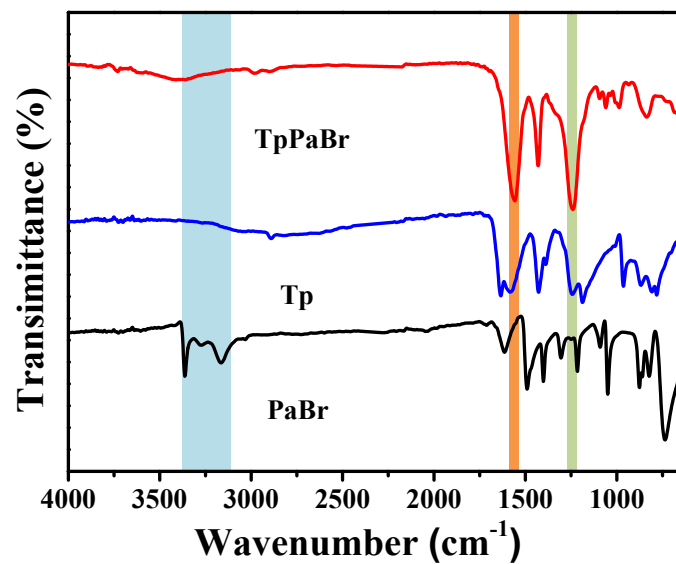


**Fig. S7.** FT-IR spectra of Tp, PaBr, and TpPaBr.

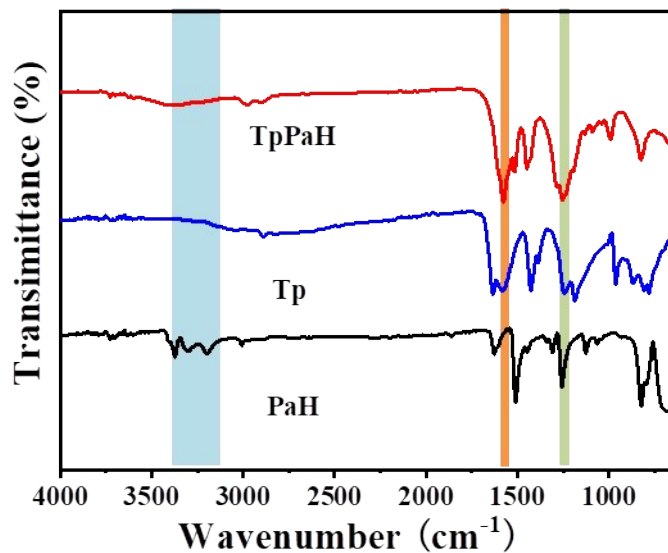


**Fig. S8.** FT-IR spectra of Tp, PaH, and TpPaH.

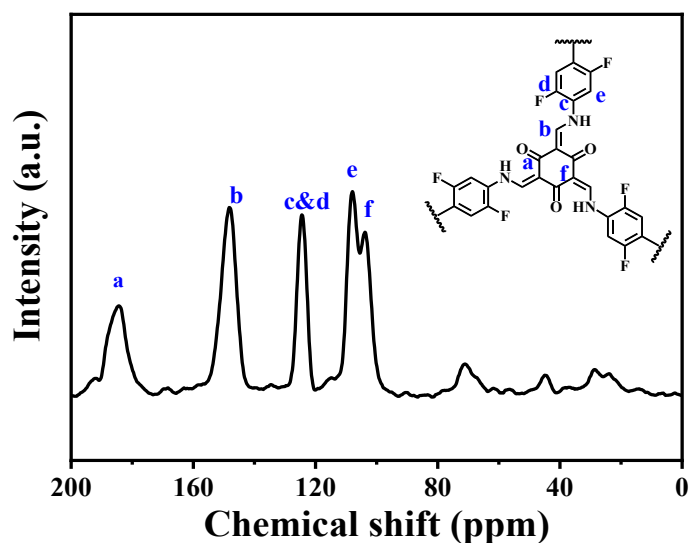


**Fig. S9.** Solid-state  $^{13}\text{C}$  CP/MAS NMR spectrum of TpPaF.

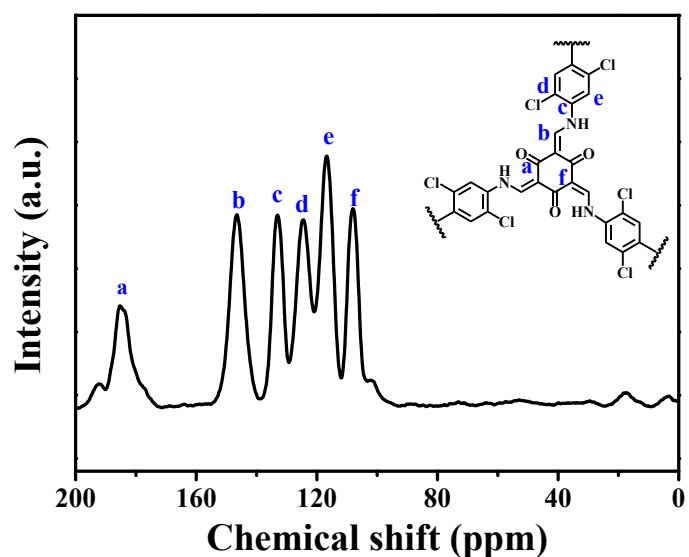


**Fig. S10.** Solid-state  $^{13}\text{C}$  CP/MAS NMR spectrum of TpPaCl.

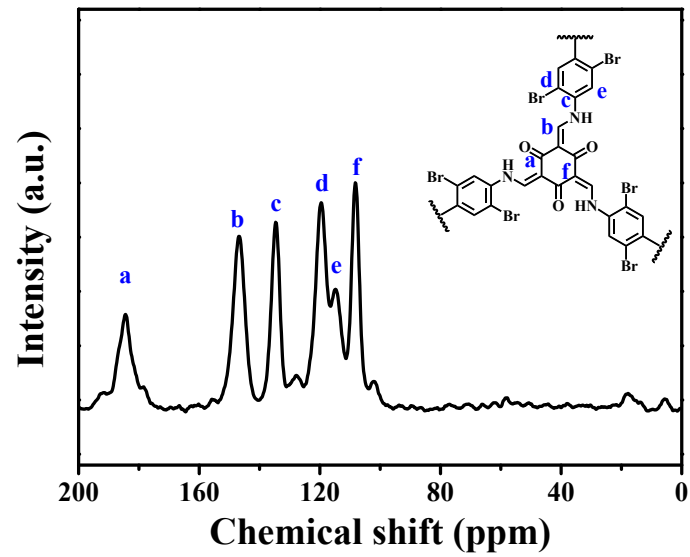


**Fig. S11.** Solid-state  $^{13}\text{C}$  CP/MAS NMR spectrum of TpPaBr.

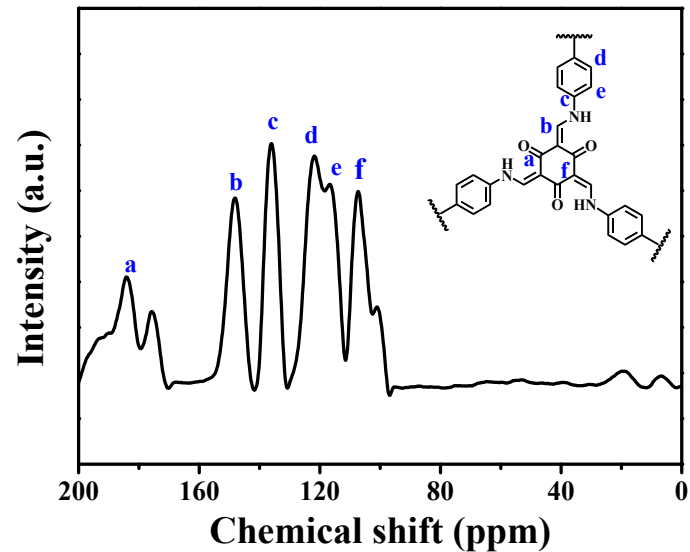


**Fig. S12.** Solid-state  $^{13}\text{C}$  CP/MAS NMR spectrum of TpPaH.

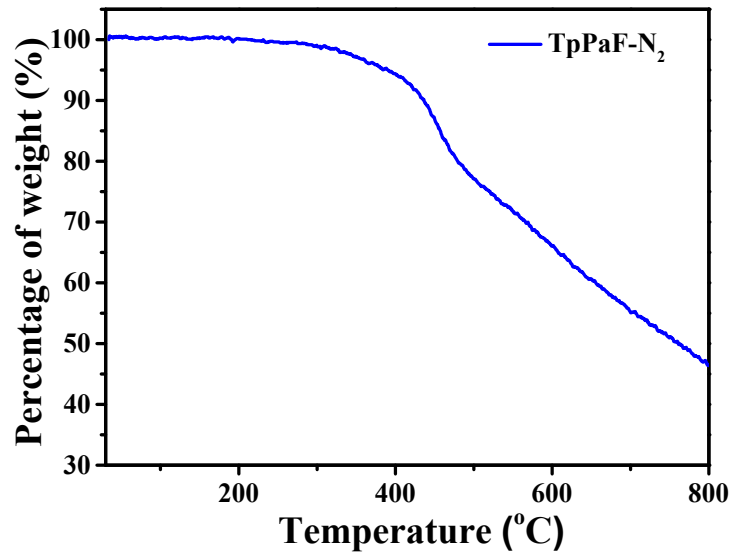


**Fig. S13.** TGA profile of TpPaF under N<sub>2</sub> atmosphere.

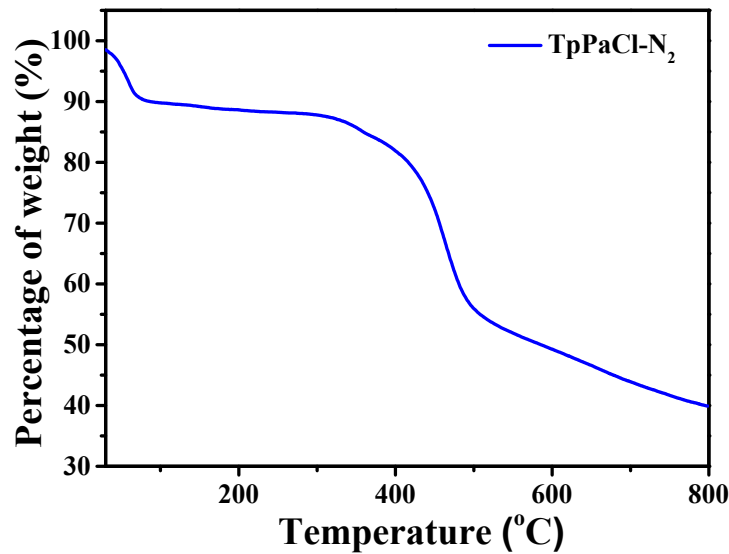


**Fig. S14.** TGA profile of TpPaCl under N<sub>2</sub> atmosphere.

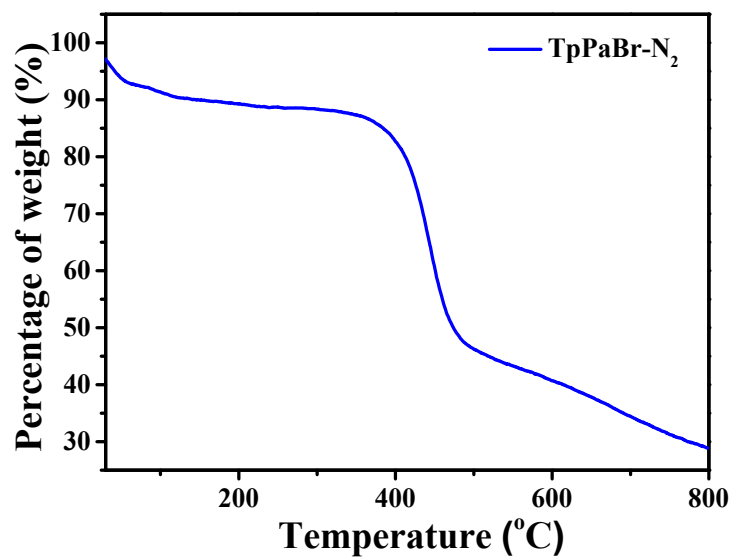


**Fig. S15.** TGA profile of TpPaBr under N<sub>2</sub> atmosphere.

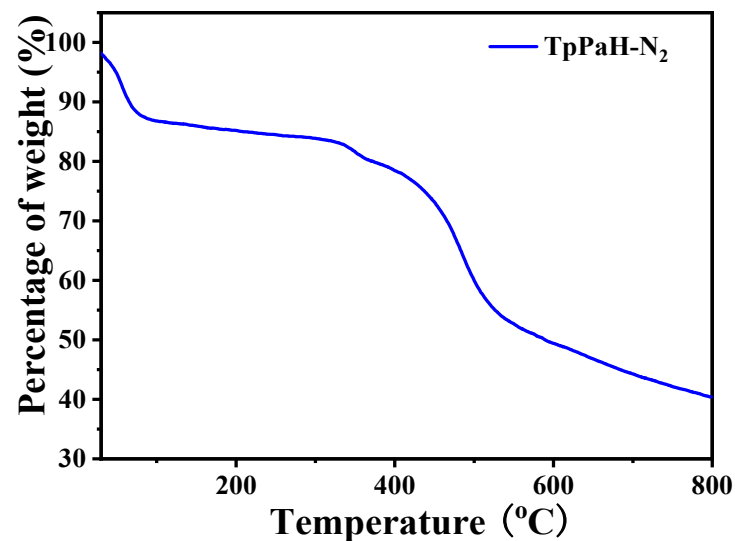


**Fig. S16.** TGA profile of TpPaH under N<sub>2</sub> atmosphere.

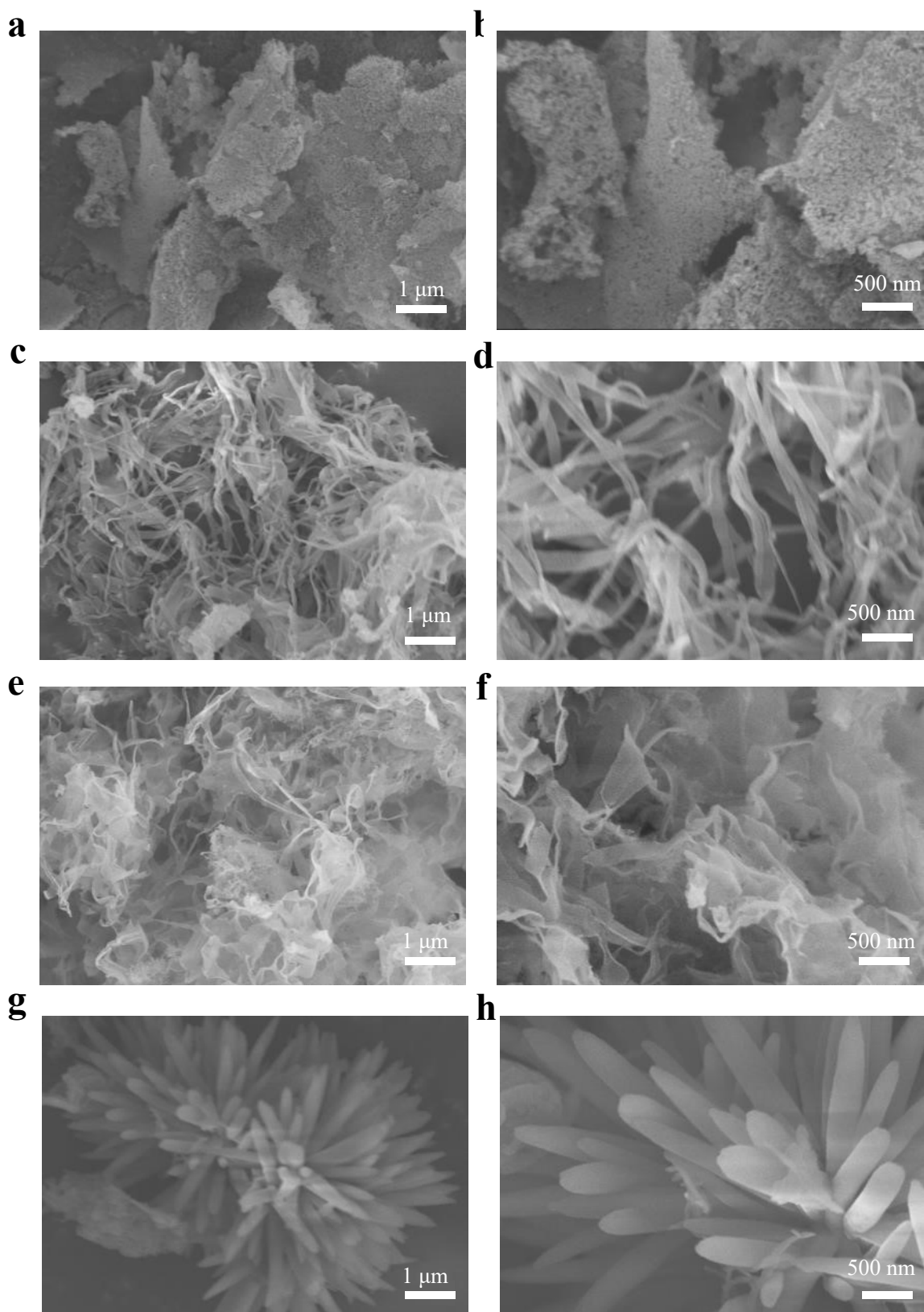


**Fig. S17.** SEM images of (a, b) TpPaF, (c, d) TpPaCl, (e, f) TpPaBr, and (g, h) TpPaH.

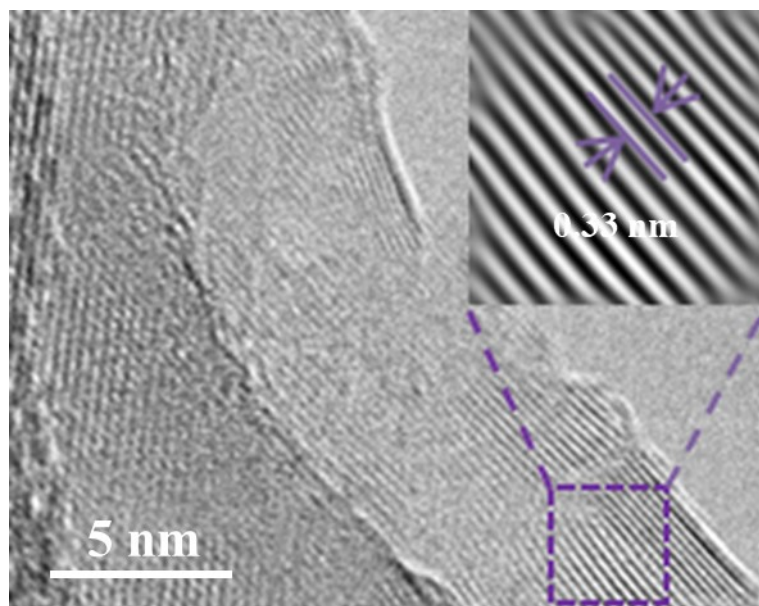


**Fig. S18.** HR-TEM and Fourier transform (FFT) images of TpPaCl.

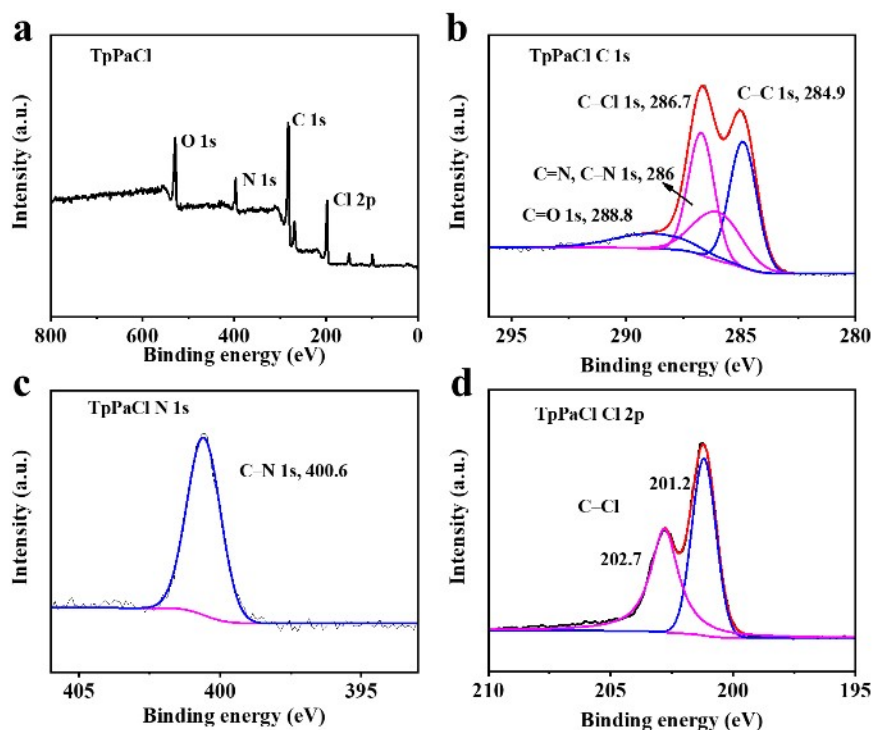


**Fig. S19.** (a) XPS survey scan spectra of TpPaCl. High resolution (b) C 1s, (c) N 1s, and (d) Cl 2p XPS spectra of TpPaCl.

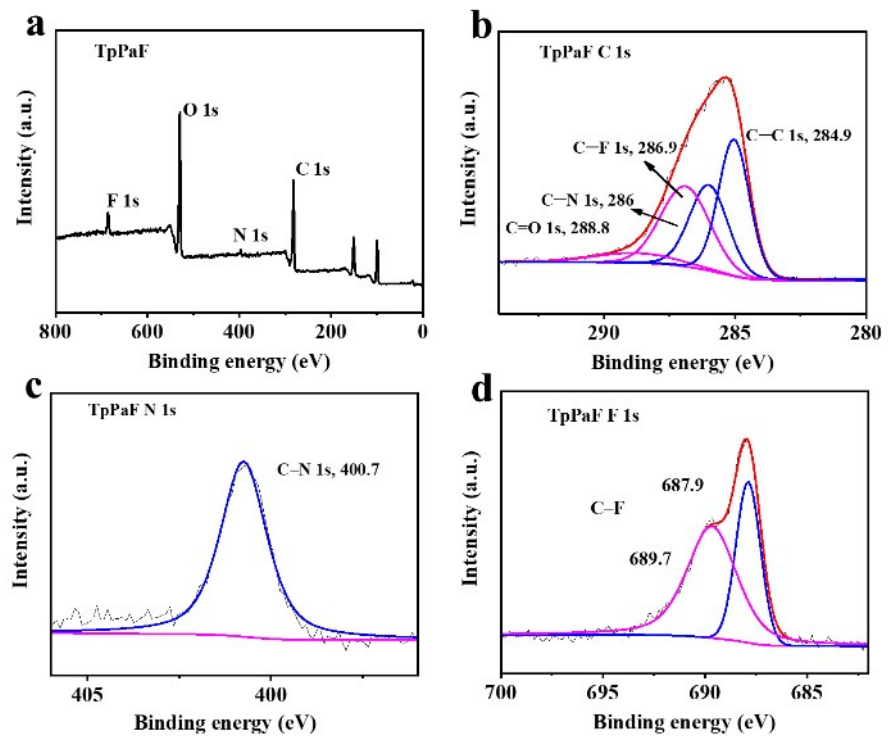


**Fig. S20.** (a) XPS survey scan spectra of TpPaF, high resolution (b) C 1s, (c) N 1s, and (d) F 1s XPS spectra of TpPaF.

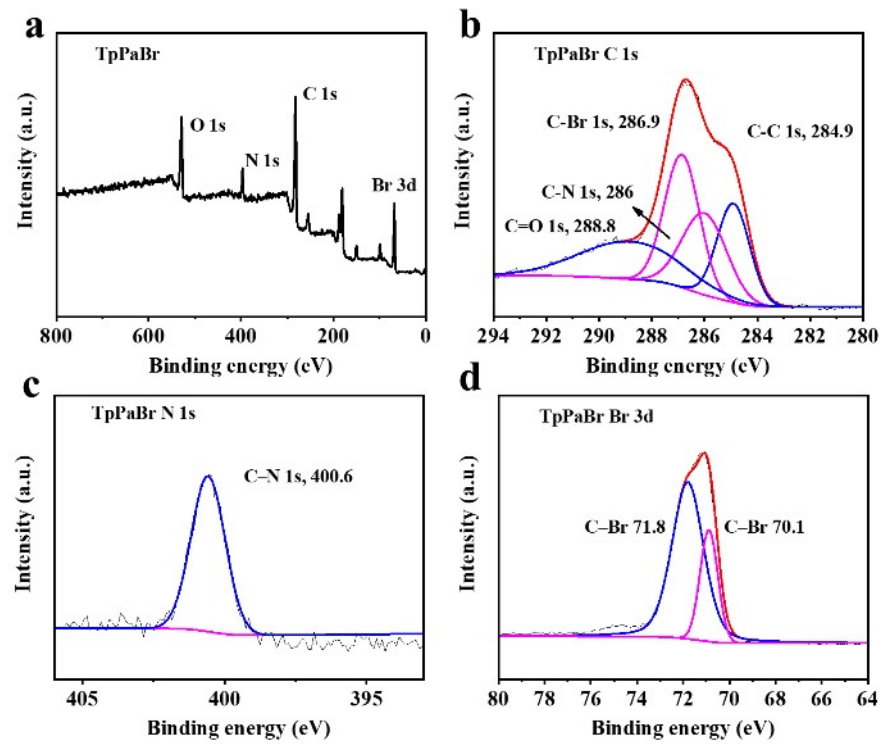


**Fig. S21.** (a) XPS survey scan spectra of TpPaBr. High resolution (b) C 1s, (c) N 1s, and (d) Br 3d XPS spectra of the TpPaBr.

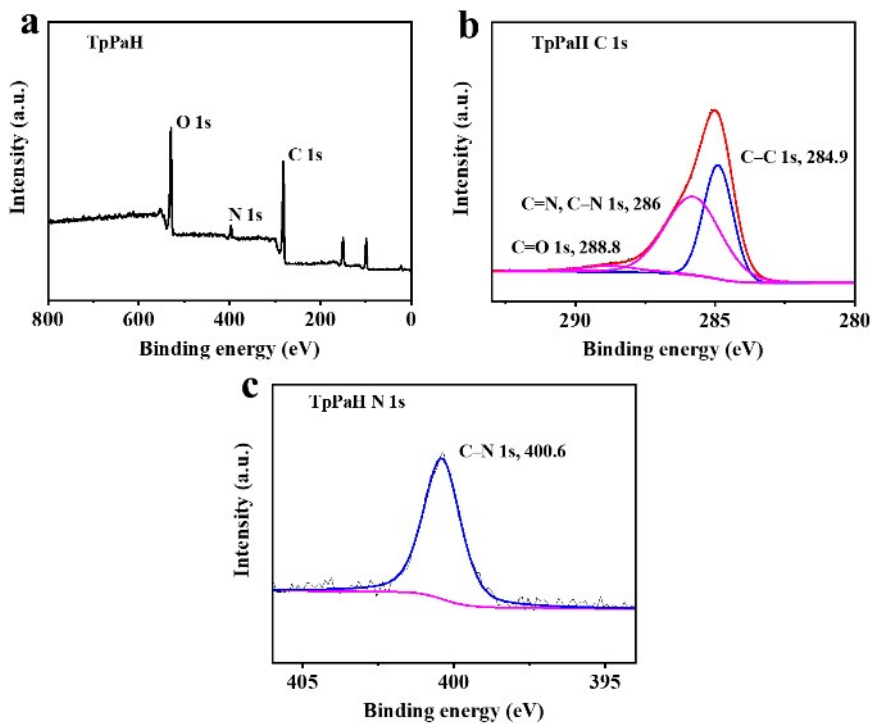


**Fig. S22.** (a) XPS survey scan spectra of TpPaH. High resolution (b) C 1s and (c) N 1s XPS spectra of the TpPaH.

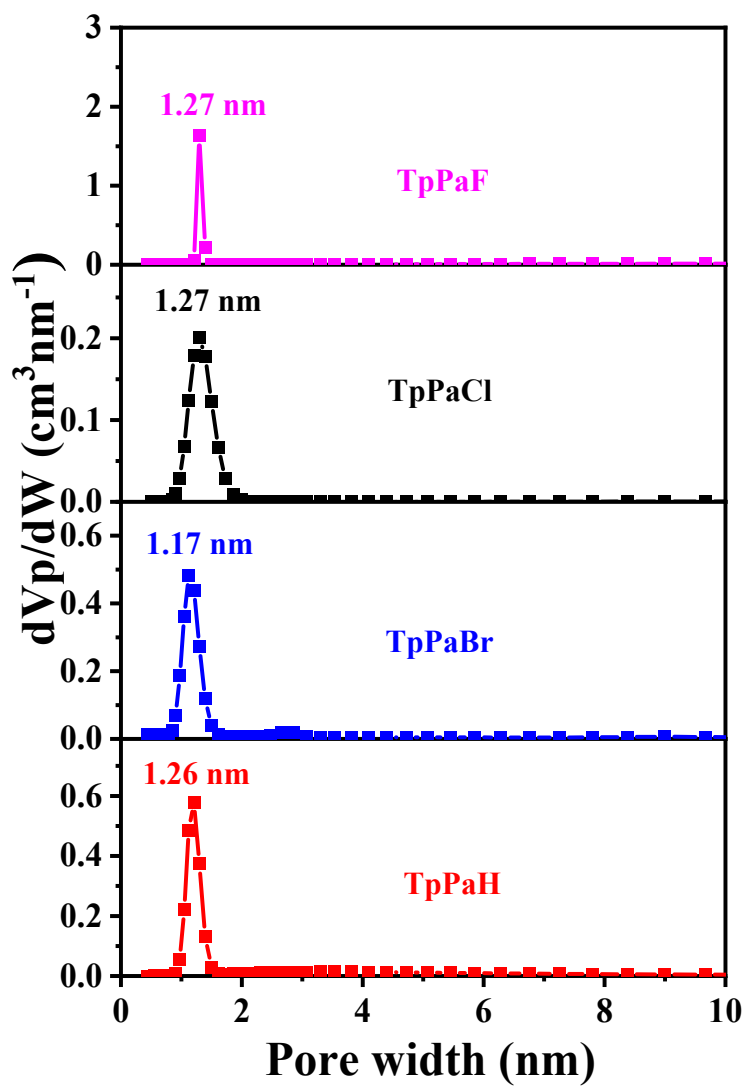


**Fig. S23.** The pore size distribution curves of (magenta) TpPaF, (black) TpPaCl, (blue) TpPaBr, and (red) TpPaH at 77 K.

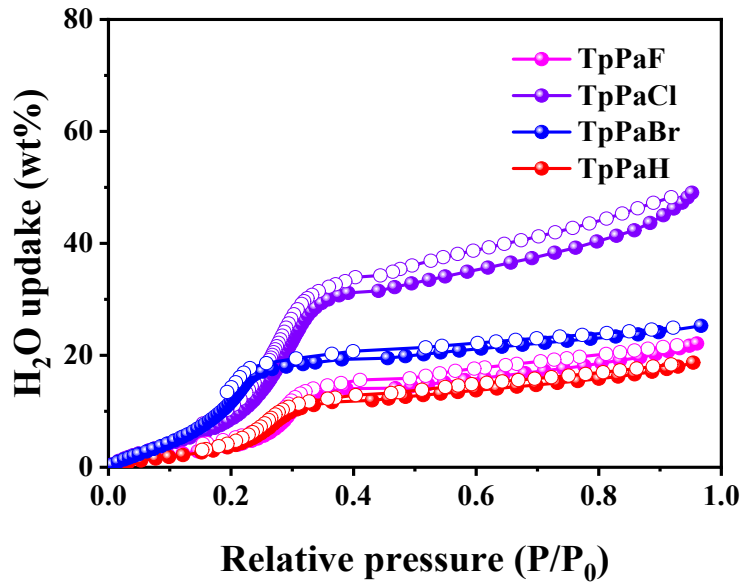


**Fig. S24.** Water adsorption isotherms (filled symbols) and desorption isotherms (open symbols) for TpPaF, TpPaCl, TpPaBr, and TpPaH at 298 K.

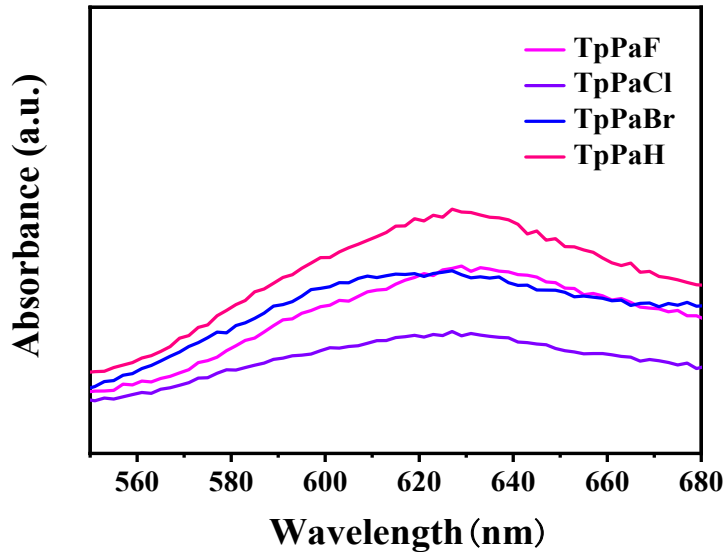


**Fig. S25.** Steady-state photoluminescence (PL) spectra of TpPaF, TpPaCl, TpPaBr, and TpPaH.

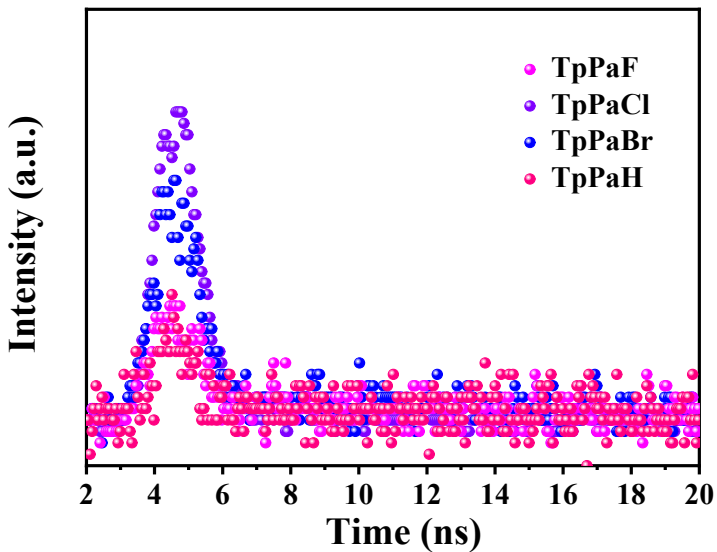


**Fig. S26.** Time-resolved PL decay spectra of TpPaF, TpPaCl, TpPaBr, and TpPaH.

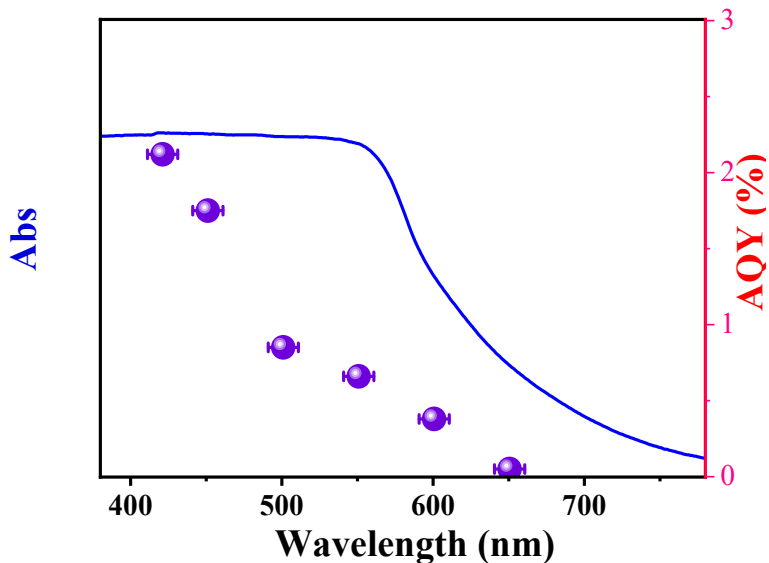


**Fig. S27.** Wavelength dependent AQE values of TpPaCl in seawater. An Xe-lamp equipped with a series of band-pass filters (420, 450, 500, 550, 600, and 650 nm) was used as the light source. Reaction conditions: 5 mg TpPaCl, 0.1 M ascorbic acid, room temperature, 5 h.

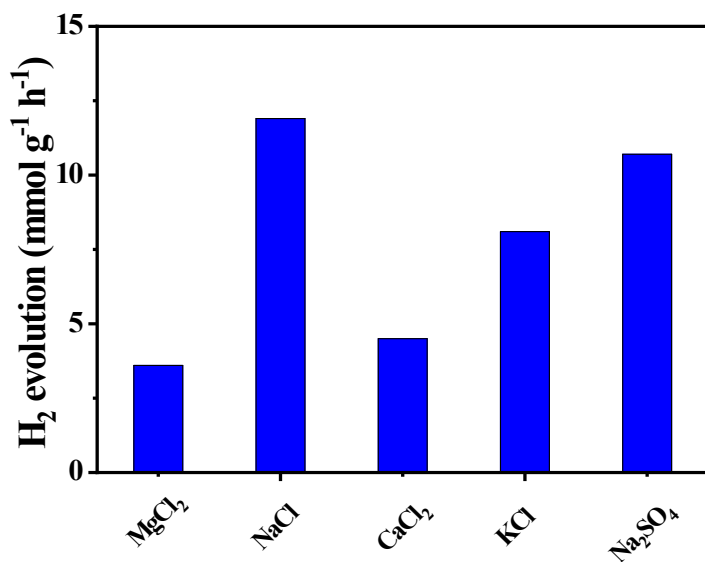


**Fig. S28.** Photocatalytic  $H_2$  evolution over TpPaCl in the presence of different salts ( $MgCl_2$ ,  $NaCl$ ,  $CaCl_2$ ,  $KCl$ , or  $Na_2SO_4$ ; 3.5 wt% in the reaction solution). Reaction conditions: 2 mg TpPaCl,  $\lambda > 420$  nm, 0.1 M ascorbic acid, room temperature, 5 h.

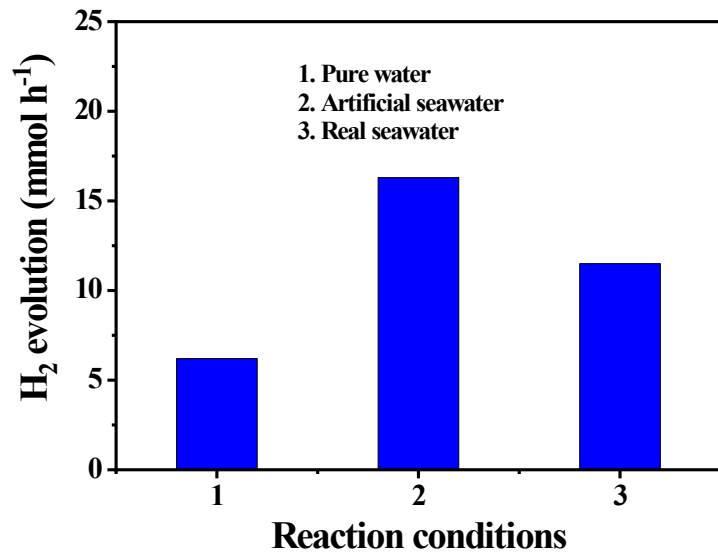


**Fig. S29.** Photocatalytic  $H_2$  evolution over TpPaCl in pure water, artificial seawater, and real seawater. Reaction conditions: Reaction conditions: 2 mg COFs,  $\lambda > 420$  nm, 0.1 M ascorbic acid, room temperature, 5 h. Real seawater was sampled from Qingdao, China, specifically from the waters of Lingshan Bay in Qingdao. The coordinates of the water collection point were 120.18.35.82, and the average water depth at the collection point was approximately 10 meters.

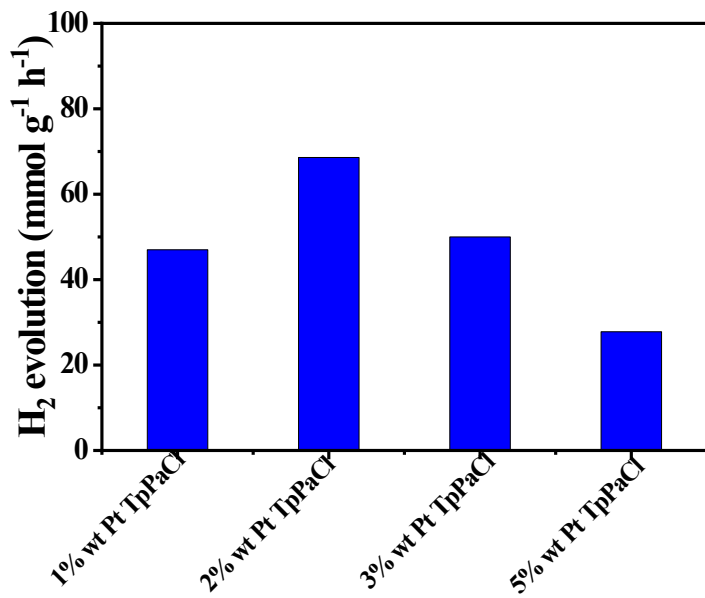


**Fig. S30.** Photocatalytic  $\text{H}_2$  evolution rates of TpPaCl in pure water with different feeding amounts of hexachloroplatinic acid aqueous solution (1 wt%, 2 wt%, 3 wt%, and 5 wt% Pt relative to TpPaCl). Reaction conditions: 5 mg TpPaCl,  $\lambda > 420$  nm, 0.1 M ascorbic acid, room temperature, 5 h.

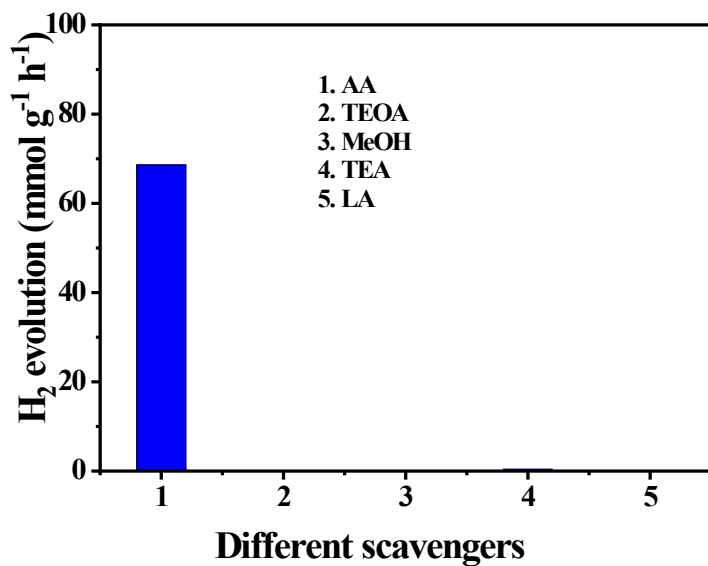


**Fig. S31.** Hydrogen evolution over TpPaCl in pure water by using different sacrificial agents. Reaction conditions: 5 mg TpPaCl, the aqueous solution containing sacrificial agent (1: 20 mL 0.1 M ascorbic acid; 2: 2 mL triethanolamine and 18 mL water; 3: 2 mL methanol and 18 mL water; 4: 2 mL trimethylamine solution and 18 mL water; 5: 2 mL lactic acid and 18 mL water).  $\lambda > 420$  nm, hexachloroplatinic acid aqueous solution (2 wt% Pt to TpPaCl), room temperature, 5 h.

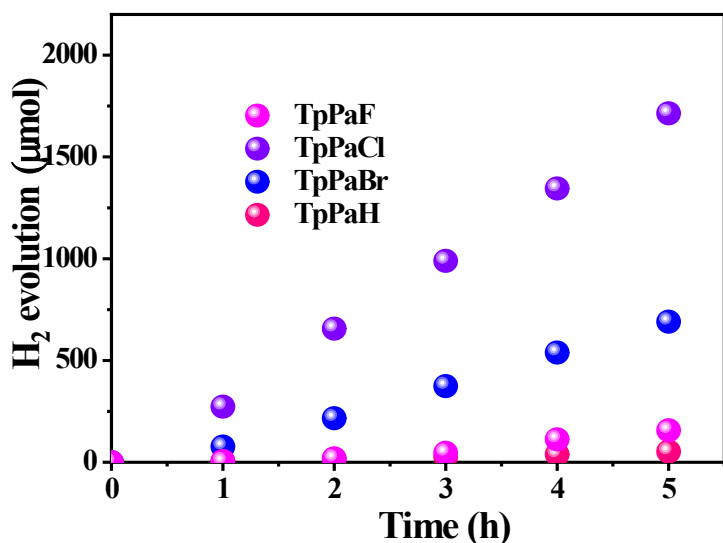


**Fig. S32.** Time-resolved photocatalytic H<sub>2</sub> evolution over TpPaF, TpPaCl, TpPaBr, and TpPaH in pure water under  $\lambda > 420$  nm irradiation. Reaction conditions: 5 mg TpPaX,  $\lambda > 420$  nm, 0.1 M ascorbic acid, hexachloroplatinic acid aqueous solution (2 wt% Pt to photocatalyst), room temperature, 5 h.

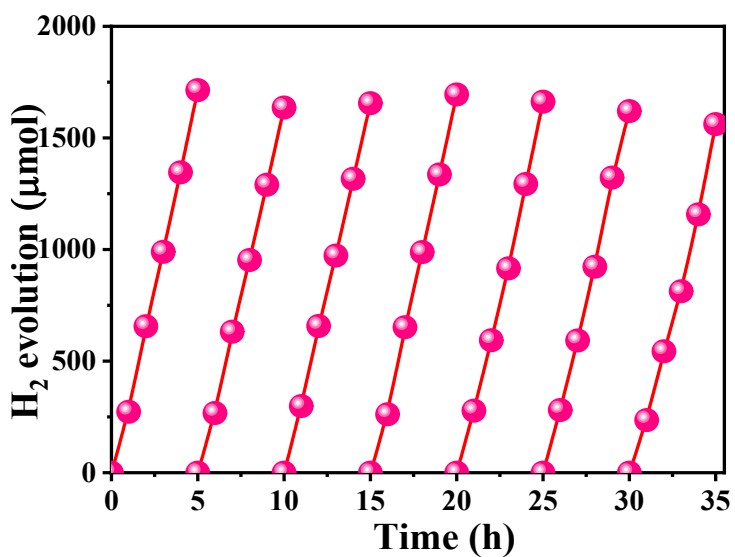


**Fig. S33.** Plot showing longer-term photocatalytic hydrogen evolution in pure water for TpPaCl under visible light irradiation. Reaction conditions: 5 mg TpPaCl,  $\lambda > 420$  nm, 0.1 M ascorbic acid, hexachloroplatinic acid aqueous solution (2 wt% Pt to TpPaCl), room temperature, 35 h.

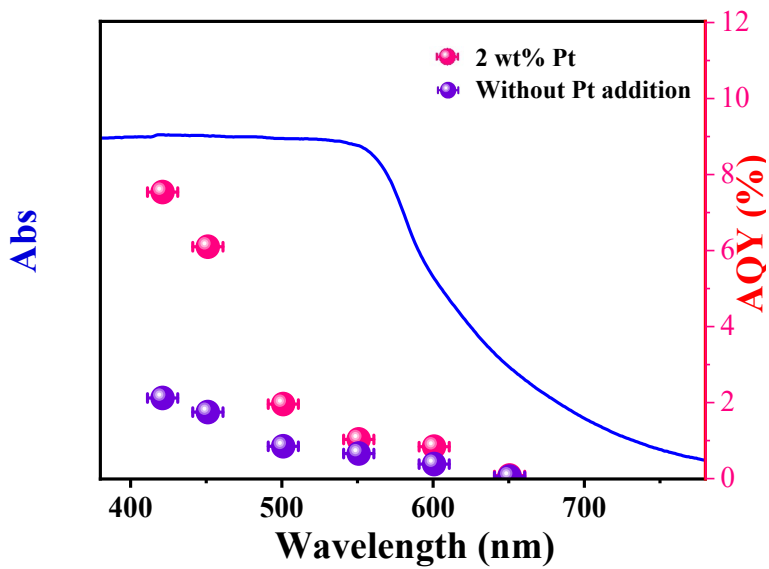


**Fig. S34.** Wavelength dependent AQE values of TpPaCl in pure water (pink) and seawater (purple). An Xe-lamp equipped with a series of band-pass flitters (420, 450, 500, 550, 600, and 650 nm) was used as the light source. Reaction conditions: 5 mg TpPaCl, 0.1 M ascorbic acid, hexachloroplatinic acid aqueous solution (2 wt% Pt to TpPaCl), room temperature, 5 h.

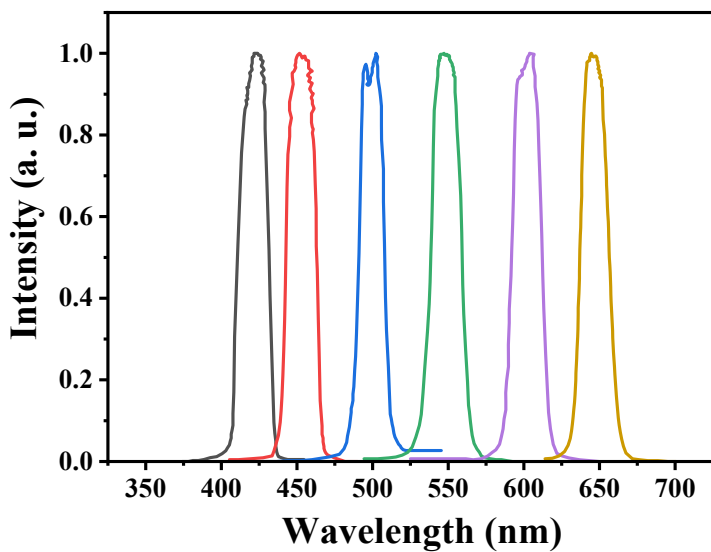


**Fig. S35.** UV-vis spectra of the filters (420, 450, 500, 550, 600, and 650 nm).

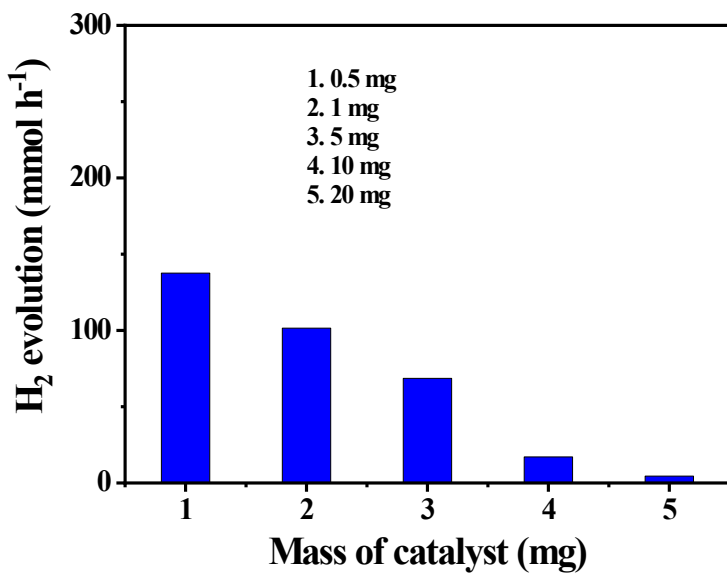


**Fig. S36.** Photocatalytic  $\text{H}_2$  evolution over TpPaCl in pure water by using different catalyst dosages. Reaction conditions:  $\lambda > 420 \text{ nm}$ , 0.1 M ascorbic acid, hexachloroplatinic acid aqueous solution (2 wt% Pt relative to TpPaCl), room temperature, 5 h.

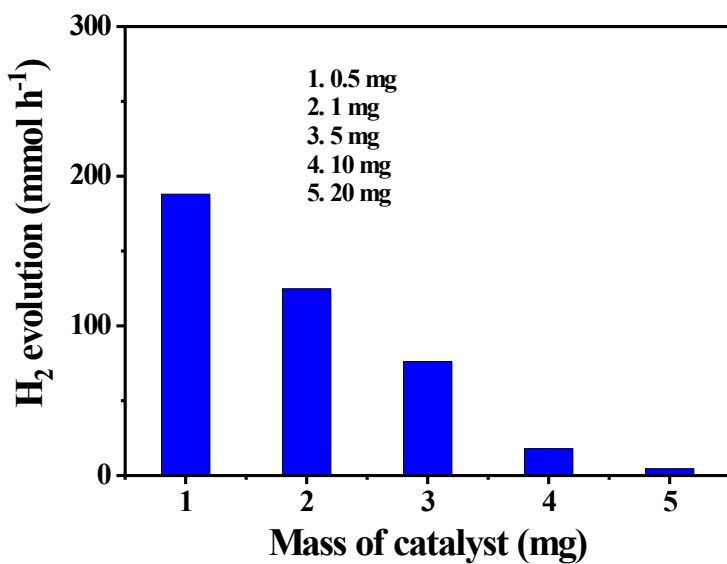


**Fig. S37.** Photocatalytic  $H_2$  evolution over TpPaCl in seawater by using different catalyst dosages. Reaction conditions:  $\lambda > 420 \text{ nm}$ , 0.1 M ascorbic acid, hexachloroplatinic acid aqueous solution (2 wt% Pt relative to TpPaCl), room temperature, 5 h.

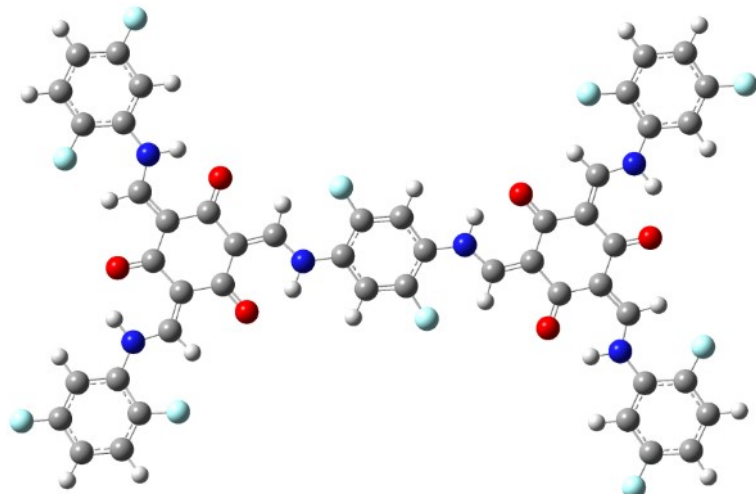


**Fig. S38.** Optimized geometrical structure of the representative fragment of TpPaF.

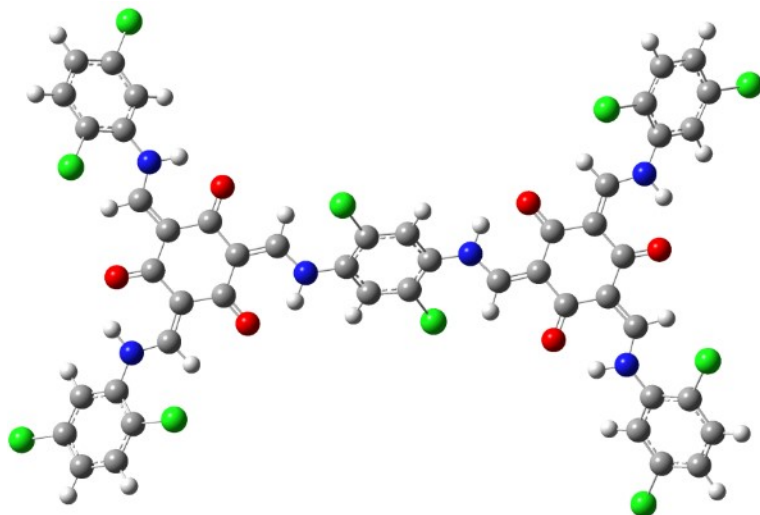


**Fig. S39.** Optimized geometrical structure of the representative fragment of TpPaCl.

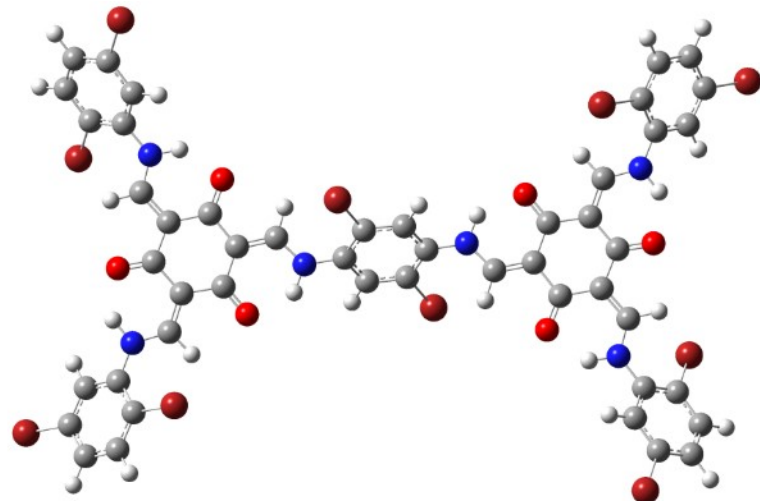


**Fig. S40.** Optimized geometrical structure of the representative fragment of TpPaBr.

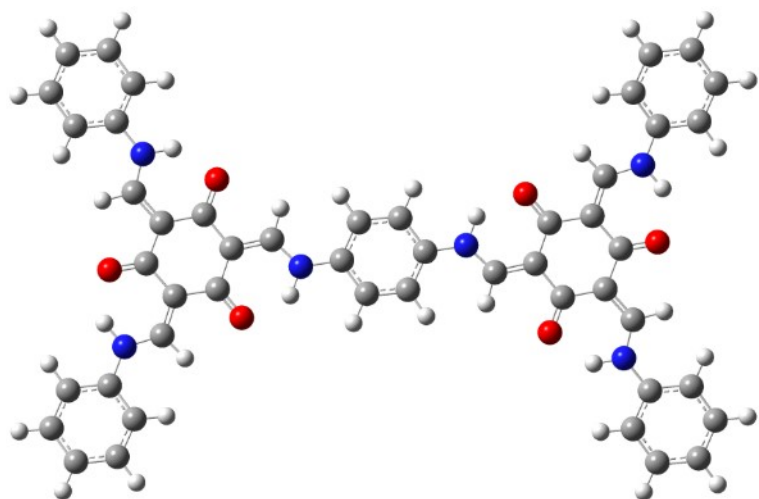


**Fig. S41.** Optimized geometrical structure of the representative fragment of TpPaH.

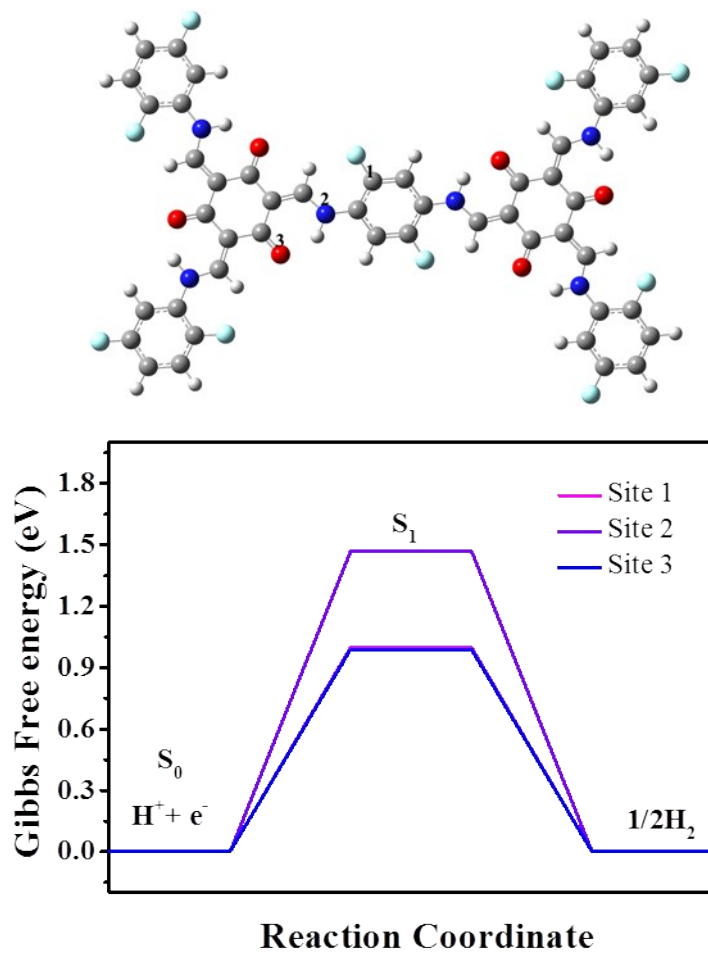


**Fig. S42.** The calculated free energies (eV) at different active sites of HER on TpPaF via the single-site process. Grey balls: C; white balls: H; red balls: O; blue balls: N; Indigo balls: F.

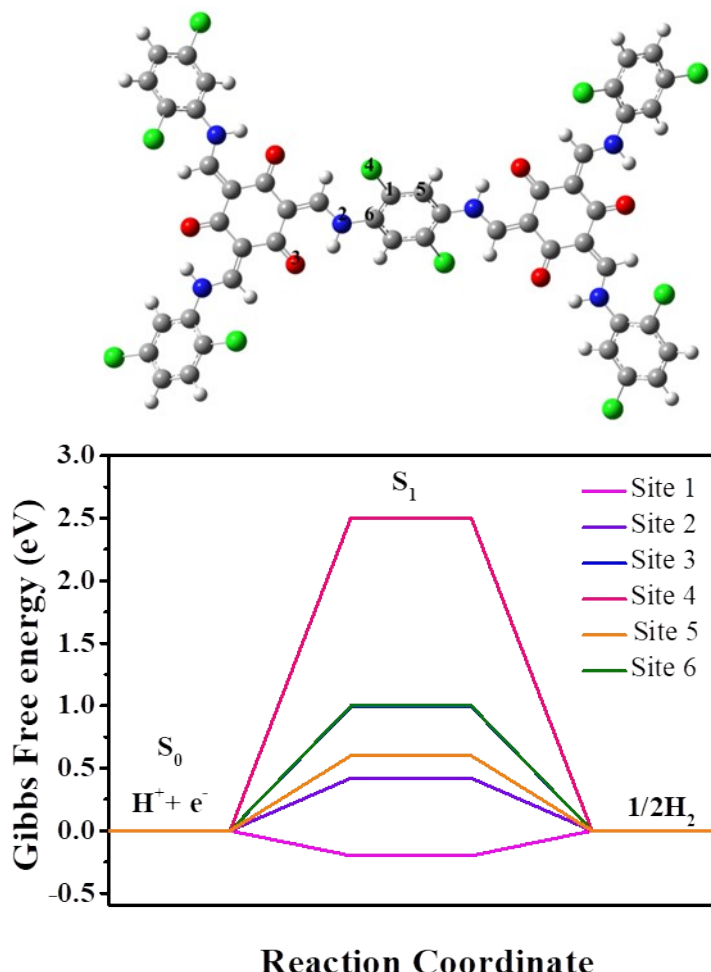


**Fig. S43.** The calculated free energies (eV) at different active sites of HER on TpPaCl *via* the single-site process. Grey balls: C; white balls: H; red balls: O; blue balls: N; green balls: Cl.

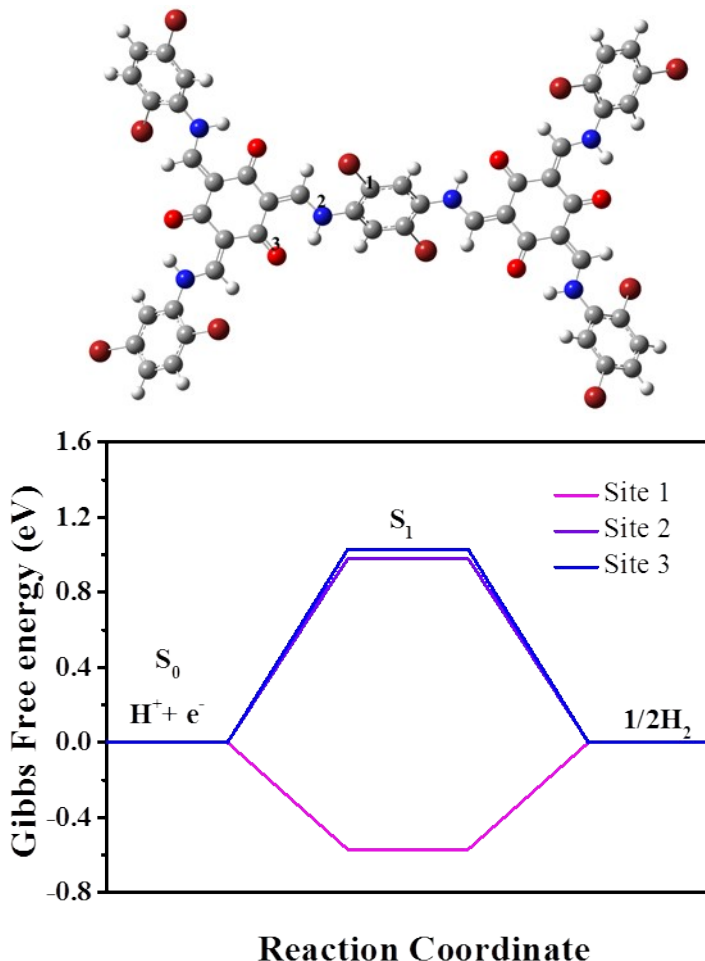


**Fig. S44.** The calculated free energies (eV) at different active sites of HER on TpPaBr *via* the single-site process. Grey balls: C; white balls: H; red balls: O; blue balls: N; maroon balls: Br.

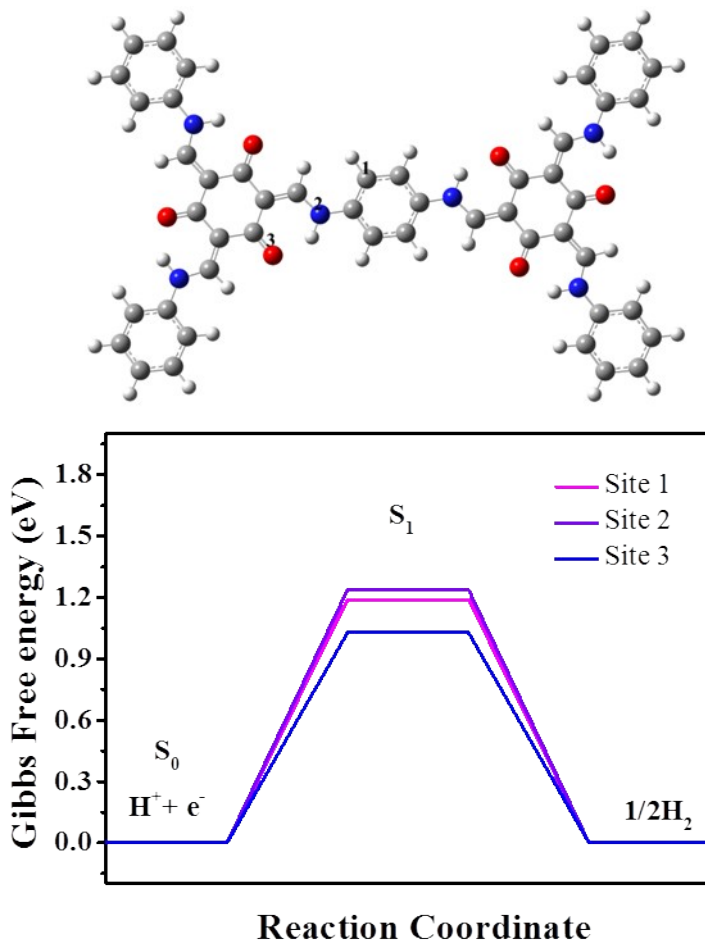


**Fig. S45.** The calculated free energies (eV) at different active sites of HER on TpPaH *via* the single-site process. Grey balls: C; white balls: H; red balls: O; blue balls: N.

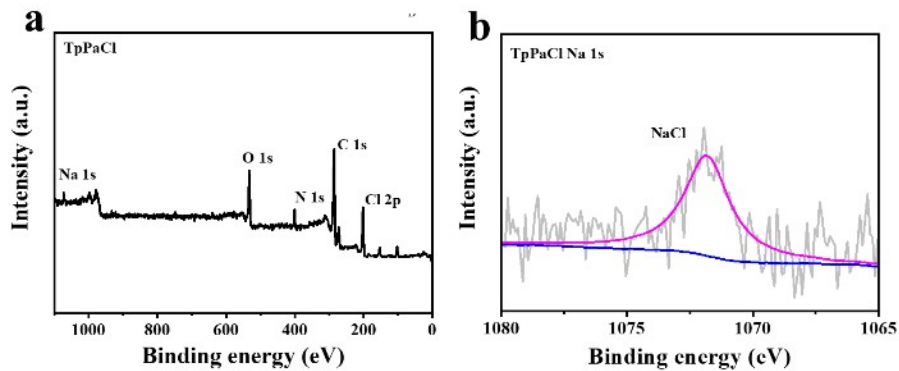


**Fig. S46.** (a) Survey scan XPS spectra of TpPaCl after adsorption of NaCl. High resolution (b) Na 1s XPS spectra of the TpPaCl after adsorption of NaCl.

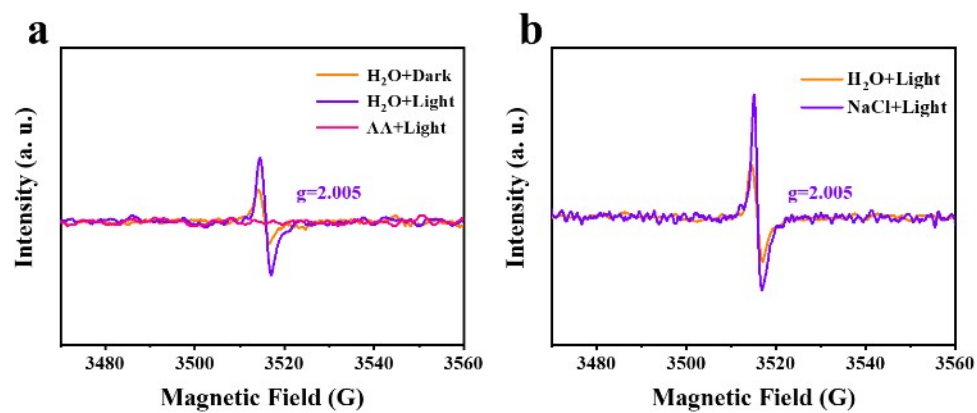


**Fig. S47.** (a) ESR signal of TpPaCl in  $\text{H}_2\text{O}$  under darkness,  $\text{H}_2\text{O}$  under visible light illumination, and 0.1 M AA solution under visible light illumination, respectively. (b) ESR signal of TpPaCl in  $\text{H}_2\text{O}$  and 3.5 wt% NaCl solution under visible light illumination.

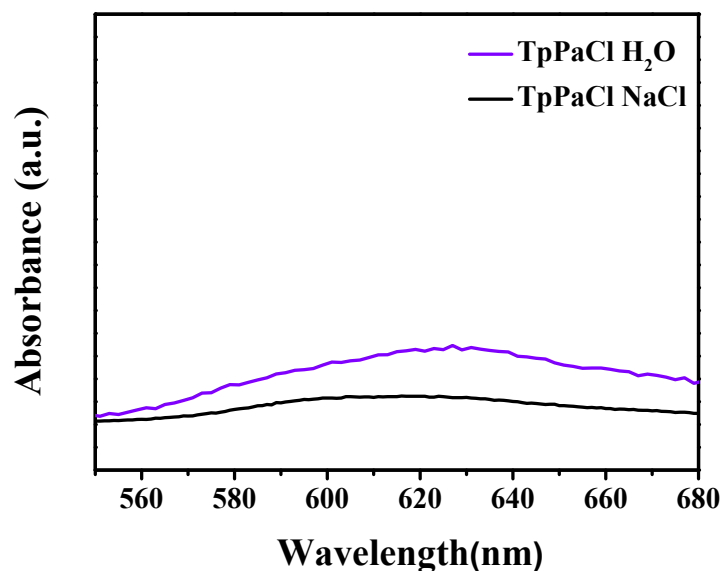


**Fig. S48.** Steady-state photoluminescence (PL) spectra of TpPaCl in  $\text{H}_2\text{O}$  and aqueous NaCl solution, respectively.

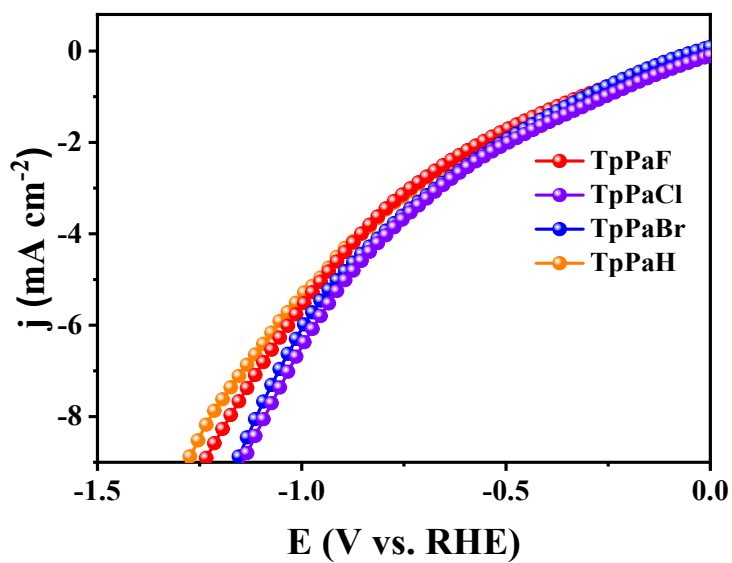


**Fig. S49.** HER polarization curves of TpPaX (X=F, Cl, Br, H).

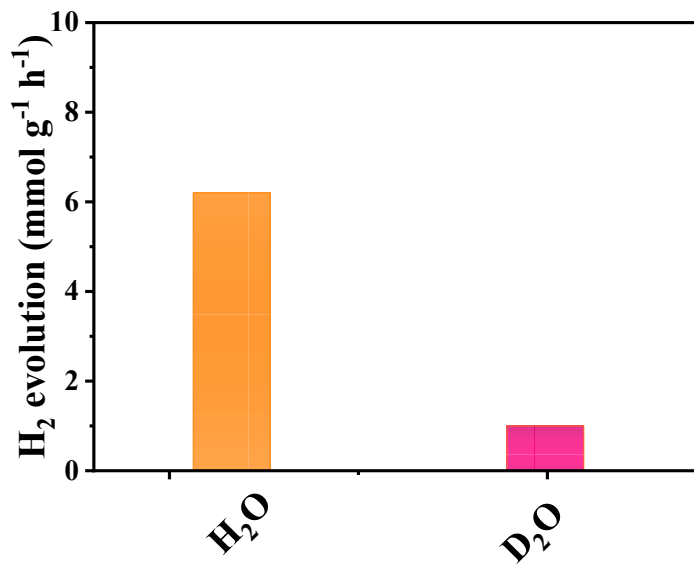


**Fig. S50.** Kinetic isotopic effects of HER over TpPaCl in H<sub>2</sub>O and D<sub>2</sub>O. Reaction conditions: 2 mg TpPaCl,  $\lambda > 420$  nm, 0.1 M ascorbic acid, room temperature, 5 h.

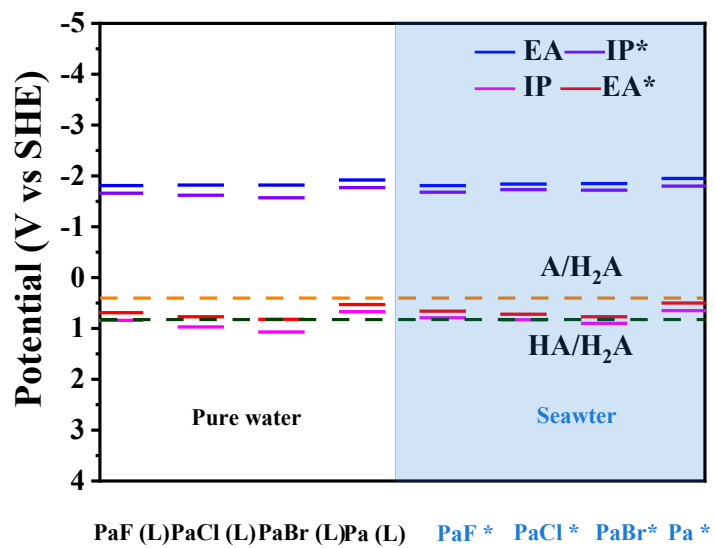


**Fig. S51.** (TD-)DFT calculation predicted ionization potential (IP), electron affinity (EA), and excited states (IP\* and EA\*) on the cut-out cluster models in pure water and seawater.

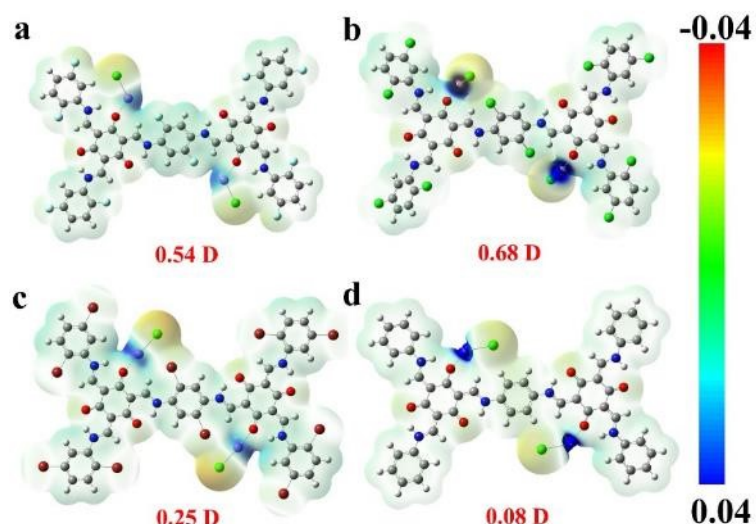


**Fig. S52.** The electrostatic potential distribution of (a) TpPaF, (b) TpPaCl, (c) TpPaBr, and (d) TpPaH in sweater.

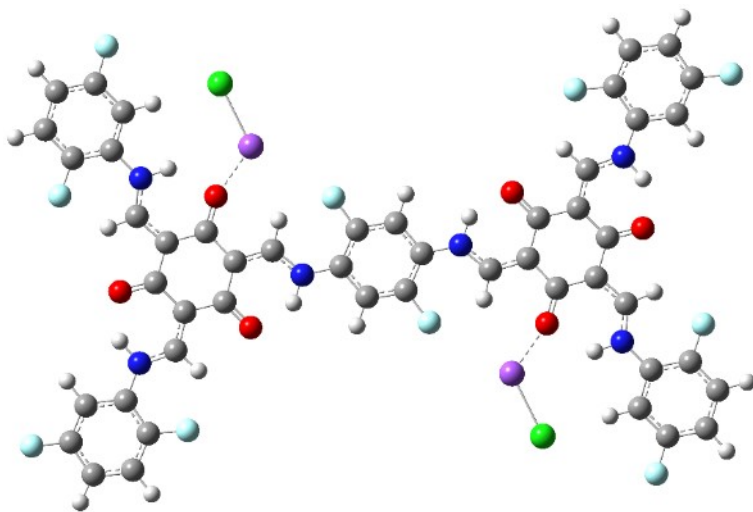


**Fig. S53.** Optimized geometrical structure of the representative fragment of TpPaF-NaCl.

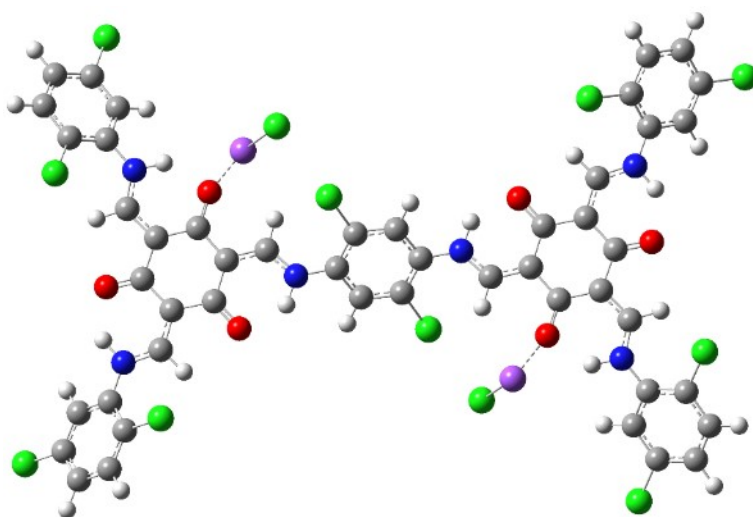


**Fig. S54.** Optimized geometrical structure of the representative fragment of TpPaCl-NaCl.

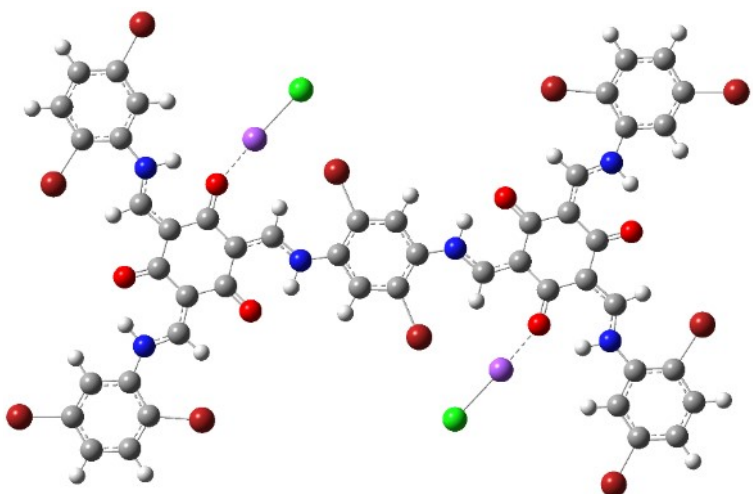


**Fig. S55.** Optimized geometrical structure of the representative fragment of TpPaBr-NaCl.

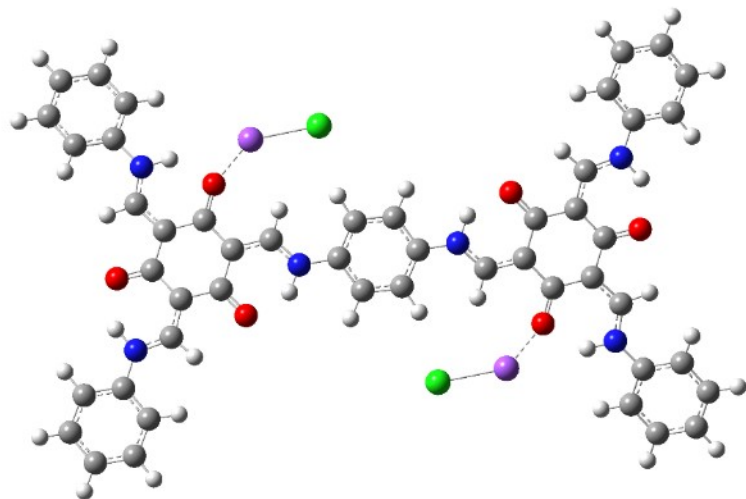


**Fig. S56.** Optimized geometrical structure of the representative fragment of TpPaH-NaCl.

**Table S1.** ICP-MS analysis

Sample	Entry	Pd (wt.%)	Pt (wt.%)	Au (wt.%)
<b>TpPaCl</b>	1	0.00005	0.00001	0.00002
	2	0.00005	0.00001	0.00002
	3	0.00005	0.00001	0.00002

**Table S2.** Fractional atomic coordination for the Pawley-refined TpPaF

TpPaF: Space group symmetry $P6/M$							
$a = b = 22.86 \text{ \AA}$ , $c = 3.47 \text{ \AA}$							
$\alpha = \beta = 90^\circ$ , $\gamma = 120^\circ$							
Atom	x ( $\text{\AA}$ )	y ( $\text{\AA}$ )	z ( $\text{\AA}$ )	Atom	x ( $\text{\AA}$ )	y ( $\text{\AA}$ )	z ( $\text{\AA}$ )
C1	0.543487	-0.026157	0	N1	0.550017	0.141453	0
C2	0.570063	0.043717	0	N2	-0.141453	0.408563	0
C3	0.526233	0.070397	0	N3	-0.408563	-0.550017	0
C4	0.69284	0.407025	0	N4	-0.550017	-0.141453	0
C5	0.618707	0.359463	0	N5	0.141453	-0.408563	0
C6	0.807103	0.426637	0	N6	0.408563	0.550017	0
C7	0.026157	0.569643	0	O1	0.753045	0.285095	0
C8	-0.043717	0.526347	0	O2	-0.285095	0.46795	0
C9	-0.070397	0.455837	0	O3	-0.46795	-0.753045	0
C10	-0.407025	0.285815	0	O4	-0.753045	-0.285095	0
C11	-0.359463	0.259243	0	O5	0.285095	-0.46795	0
C12	-0.426637	0.380467	0	O6	0.46795	0.753045	0
C13	-0.569643	-0.543487	0	F1	0.638107	0.084263	0
C14	-0.526347	-0.570063	0	F2	-0.08426	0.553843	0
C15	-0.455837	-0.526233	0	F3	-0.55384	-0.63811	0
C16	-0.285815	-0.69284	0	F4	-0.63811	-0.08426	0
C17	-0.259243	-0.618707	0	F5	0.084263	-0.55384	0
C18	-0.380467	-0.807103	0	F6	0.553843	0.638107	0
C19	-0.543487	0.026157	0	H1	0.579583	-0.046953	0
C20	-0.570063	-0.043717	0	H2	0.824933	0.482967	0
C21	-0.526233	-0.070397	0	H3	0.512268	0.158425	0
C22	-0.69284	-0.407025	0	H4	0.046953	0.626537	0
C23	-0.618707	-0.359463	0	H5	-0.482967	0.341967	0
C24	-0.807103	-0.426637	0	H6	-0.158425	0.353843	0
C25	-0.026157	-0.569643	0	H7	-0.626537	-0.579583	0
C26	0.043717	-0.526347	0	H8	-0.341967	-0.824933	0
C27	0.070397	-0.455837	0	H9	-0.353843	-0.512268	0
C28	0.407025	-0.285815	0	H10	-0.579583	0.046953	0
C29	0.359463	-0.259243	0	H11	-0.824933	-0.482967	0
C30	0.426637	-0.380467	0	H12	-0.512268	-0.158425	0
C31	0.569643	0.543487	0	H13	-0.046953	-0.626537	0
C32	0.526347	0.570063	0	H14	0.482967	-0.341967	0
C33	0.455837	0.526233	0	H15	0.158425	-0.353843	0
C34	0.285815	0.69284	0	H16	0.626537	0.579583	0
C35	0.259243	0.618707	0	H17	0.341967	0.824933	0
C36	0.380467	0.807103	0	H18	0.353843	0.512268	0

**Table S3.** Fractional atomic coordination for the Pawley-refined TpPaCl

TpPaCl: Space group symmetry <i>P</i> 6/M							
	a = b = 22.95 Å, c = 3.51 Å						
	$\alpha = \beta = 90^\circ, \gamma = 120^\circ$						
Atom	x (Å)	y (Å)	z (Å)	Atom	x (Å)	y (Å)	z (Å)
C1	0.540887	-0.028497	0	N1	0.553433	0.141797	0
C2	0.570393	0.041457	0	N2	-0.141797	0.411637	0
C3	0.528827	0.070723	0	N3	-0.411637	-0.553433	0
C4	0.691443	0.406517	0	N4	-0.553433	-0.141797	0
C5	0.617827	0.358053	0	N5	0.141797	-0.411637	0
C6	0.806025	0.42827	0	N6	0.411637	0.553433	0
C7	0.028497	0.569383	0	O1	0.754673	0.287647	0
C8	-0.041457	0.528937	0	O2	-0.287647	0.467027	0
C9	-0.070723	0.458103	0	O3	-0.467027	-0.754673	0
C10	-0.406517	0.284927	0	O4	-0.754673	-0.287647	0
C11	-0.358053	0.259773	0	O5	0.287647	-0.467027	0
C12	-0.42827	0.377755	0	O6	0.467027	0.754673	0
C13	-0.569383	-0.540887	0	Cl1	0.658733	0.087557	0
C14	-0.528937	-0.570393	0	Cl2	-0.087557	0.571177	0
C15	-0.458103	-0.528827	0	Cl3	-0.571177	-0.658733	0
C16	-0.284927	-0.691443	0	Cl4	-0.658733	-0.087557	0
C17	-0.259773	-0.617827	0	Cl5	0.087557	-0.571177	0
C18	-0.377755	-0.806025	0	Cl6	0.571177	0.658733	0
C19	-0.540887	0.028497	0	H1	0.575317	-0.050967	0
C20	-0.570393	-0.041457	0	H2	0.822763	0.484157	0
C21	-0.528827	-0.070723	0	H3	0.515933	0.1588	0
C22	-0.691443	-0.406517	0	H4	0.050967	0.626283	0
C23	-0.617827	-0.358053	0	H5	-0.484157	0.338607	0
C24	-0.806025	-0.42827	0	H6	-0.1588	0.357133	0
C25	-0.028497	-0.569383	0	H7	-0.626283	-0.575317	0
C26	0.041457	-0.528937	0	H8	-0.338607	-0.822763	0
C27	0.070723	-0.458103	0	H9	-0.357133	-0.515933	0
C28	0.406517	-0.284927	0	H10	-0.575317	0.050967	0
C29	0.358053	-0.259773	0	H11	-0.822763	-0.484157	0
C30	0.42827	-0.377755	0	H12	-0.515933	-0.1588	0
C31	0.569383	0.540887	0	H13	-0.050967	-0.626283	0
C32	0.528937	0.570393	0	H14	0.484157	0.338607	0
C33	0.458103	0.528827	0	H15	0.1588	-0.357133	0
C34	0.284927	0.691443	0	H16	0.626283	0.575317	0
C35	0.259773	0.617827	0	H17	0.338607	0.822763	0
C36	0.377755	0.806025	0	H18	0.357133	0.515933	0

**Table S4.** Fractional atomic coordination for the Pawley-refined TpPaBr

TpPaBr: Space group symmetry $P6/M$							
$a = b = 25.26 \text{ \AA}$ , $c = 3.56 \text{ \AA}$							
$\alpha = \beta = 90^\circ$ , $\gamma = 120^\circ$							
Ato m	x ( $\text{\AA}$ )	y ( $\text{\AA}$ )	z ( $\text{\AA}$ )	Ato m	x ( $\text{\AA}$ )	y ( $\text{\AA}$ )	z ( $\text{\AA}$ )
C1	0.544198	0.977417	0	N1	0.556818	0.142702	0
C2	0.57389	0.041724	0	N2	-0.1427	0.414116	0
C3	0.532057	0.071172	0	N3	-0.41412	-0.55682	0
C4	0.695662	0.409015	0	N4	-0.55682	-0.1427	0
C5	0.621577	0.360241	0	N5	0.142702	-0.41412	0
C6	0.810979	0.430912	0	N6	0.414116	0.556818	0
C7	-0.97742	-0.43322	0	O1	0.759301	0.289391	0
C8	-0.04172	0.532166	0	O2	-0.28939	0.46991	0
C9	-0.07117	0.460885	0	O3	-0.46991	-0.7593	0
C10	-0.40902	0.286647	0	O4	-0.7593	-0.28939	0
C11	-0.36024	0.261336	0	O5	0.289391	-0.46991	0
C12	-0.43091	0.380067	0	O6	0.46991	0.759301	0
C13	0.433219	-0.5442	0	Br1	0.662791	0.088121	0
C14	-0.53217	-0.57389	0	Br2	-0.08812	0.57467	0
C15	-0.46089	-0.53206	0	Br3	-0.57467	-0.66279	0
C16	-0.28665	-0.69566	0	Br4	-0.66279	-0.08812	0
C17	-0.26134	-0.62158	0	Br5	0.088121	-0.57467	0
C18	-0.38007	-0.81098	0	Br6	0.57467	0.662791	0
C19	-0.5442	-0.97742	0	H1	0.57864	0.957806	0
C20	-0.57389	-0.04172	0	H2	0.532057	0.071172	0
C21	-0.53206	-0.07117	0	H3	0.825498	0.483867	0
C22	-0.69566	-0.40902	0	H4	0.522515	0.160864	0
C23	-0.62158	-0.36024	0	H5	-0.95781	-0.37917	0
C24	-0.81098	-0.43091	0	H6	-0.07117	0.460885	0
C25	0.977417	0.433219	0	H7	-0.48387	0.34163	0
C26	0.041724	-0.53217	0	H8	-0.16086	0.361651	0
C27	0.071172	-0.46089	0	H9	0.379166	-0.57864	0
C28	0.409015	-0.28665	0	H10	-0.46089	-0.53206	0
C29	0.360241	-0.26134	0	H11	-0.34163	-0.8255	0
C30	0.430912	-0.38007	0	H12	-0.36165	-0.52252	0
C31	-0.43322	0.544198	0	H13	-0.57864	-0.95781	0
C32	0.532166	0.57389	0	H14	-0.53206	-0.07117	0
C33	0.460885	0.532057	0	H15	-0.8255	-0.48387	0
C34	0.286647	0.695662	0	H16	-0.52252	-0.16086	0
C35	0.261336	0.621577	0	H17	0.957806	0.379166	0
C36	0.380067	0.810979	0	H18	0.071172	-0.46089	0

**Table S5.** Fractional atomic coordination for the Pawley-refined TpPaH

TpPaH: Space group symmetry <i>P</i> 6/M							
	a = b = 22.76 Å, c = 3.49 Å						
	$\alpha = \beta = 90^\circ, \gamma = 120^\circ$						
Atom	x (Å)	y (Å)	z (Å)	Atom	x (Å)	y (Å)	z (Å)
C1	0.546035	-0.023708	0	C34	0.286675	0.694267	0
C2	0.569683	0.046	0	C35	0.258662	0.619567	0
C3	0.523645	0.070002	0	C36	0.383217	0.808257	0
C4	0.694267	0.407592	0	N1	0.546557	0.141015	0
C5	0.619567	0.360905	0	N2	-0.141015	0.405542	0
C6	0.808257	0.42504	0	N3	-0.405542	-0.546557	0
C7	0.023708	0.569743	0	N4	-0.546557	-0.141015	0
C8	-0.046	0.523683	0	N5	0.141015	-0.405542	0
C9	-0.070002	0.453643	0	N6	0.405542	0.546557	0
C10	-0.407592	0.286675	0	O1	0.751457	0.28249	0
C11	-0.360905	0.258662	0	O2	-0.28249	0.468967	0
C12	-0.42504	0.383217	0	O3	-0.468967	-0.751457	0
C13	-0.569743	-0.546035	0	O4	-0.751457	-0.28249	0
C14	-0.523683	-0.569683	0	O5	0.28249	-0.468967	0
C15	-0.453643	-0.523645	0	O6	0.468967	0.751457	0
C16	-0.286675	-0.694267	0	H1	0.583792	-0.042785	0
C17	-0.258662	-0.619567	0	H2	0.626555	0.083583	0
C18	-0.383217	-0.808257	0	H3	0.827202	0.481847	0
C19	-0.546035	0.023708	0	H4	0.508502	0.157932	0
C20	-0.569683	-0.046	0	H5	0.042785	0.626577	0
C21	-0.523645	-0.070002	0	H6	-0.083583	0.542972	0
C22	-0.694267	-0.407592	0	H7	-0.481847	0.345355	0
C23	-0.619567	-0.360905	0	H8	-0.157932	0.35057	0
C24	-0.808257	-0.42504	0	H9	-0.626577	-0.583792	0
C25	-0.023708	-0.569743	0	H10	-0.542972	-0.626555	0
C26	0.046	-0.523683	0	H11	-0.345355	-0.827202	0
C27	0.070002	-0.453643	0	H12	-0.35057	-0.508502	0
C28	0.407592	-0.286675	0	H13	-0.583792	0.042785	0
C29	0.360905	-0.258662	0	H14	-0.626555	-0.083583	0
C30	0.42504	-0.383217	0	H15	-0.827202	-0.481847	0
C31	0.569743	0.546035	0	H16	-0.508502	-0.157932	0
C32	0.523683	0.569683	0	H17	-0.042785	-0.626577	0
C33	0.453643	0.523645	0	H18	0.083583	-0.542972	0

**Table S6.** Elemental analysis<sup>a</sup>

Sample		C%	N%	H%	C/N
TpPaF	Calcd.	59.27	8.64	2.69	6.86
	Found	49.68	8.36	4.02	5.94
TpPaCl	Calcd.	52.14	9.6	2.99	5.43
	Found	42.33	8.01	3.77	5.28
TpPaBr	Calcd.	39.96	7.36	2.29	5.43
	Found	33.96	6.19	2.94	5.49
TpPaH	Calcd.	68.25	12.57	4.82	5.43
	Found	54.12	10.03	4.22	5.40

<sup>a</sup>The slight difference between the measured chemical composition and the theoretical values is attributed to 1) the adsorption of water that decreased the content of C and N while increased the H content; 2) the inadequate condensation of monomers that caused the slight offset of the C/N ratio.

**Table S7.** Textural properties

Sample	$S_{\text{BET}}^{\text{a}}$ ( $\text{m}^2 \text{ g}^{-1}$ )	$V_{\text{total}}^{\text{b}}$ ( $\text{cm}^3 \text{ g}^{-1}$ )	$D_{\text{av}}^{\text{c}}$ (nm)
TpPaF	452	0.83	7.3
TpPaCl	493	0.54	4.4
TpPaBr	407	0.44	4.3
TpPaH	404	0.34	3.5

<sup>a</sup>Brunauer-Emmett-Teller (BET) surface area. <sup>b</sup>Total pore volume. <sup>c</sup>Average pore size.

**Table S8.** Summary of the fluorescence lifetime<sup>a</sup>

Sample	$\tau_1$ (ns) (A <sub>1</sub> )	$\tau_2$ (ns) (A <sub>2</sub> )	$\tau_{\text{avg}}$ (ns) (A)
TpPaF	0.68 (55.49%)	6.77 (44.51%)	3.4
TpPaCl	0.53 (23.09%)	20 (76.91%)	15.5
TpPaBr	0.60 (36.28%)	20 (63.72%)	13.0
TpPaH	0.51 (59.39%)	3.11 (40.61%)	1.6

<sup>a</sup>A<sub>1</sub>+A<sub>2</sub>=1.

**Table S9.** Hydrogen evolution performance without co-catalysts

Photocatalyst	Illumination	SED	Solution	Activity		Ref.
				( $\mu\text{mol g}^{-1} \text{h}^{-1}$ )	AQE (%)	
TpPaCl	$\lambda > 420 \text{ nm}$	AA	seawater	16300 <sup>a</sup>	2.12 (420 nm)	This work
ZnPor-DETH-COF	$\lambda > 420 \text{ nm}$	TEOA	pure water	403	0.063 (450 nm)	[2]
BT-COF	$\lambda > 420 \text{ nm}$	AA	pure water	7700	7.53 (420 nm)	[3]
Py-ClTP-BT-COF	$\lambda > 420 \text{ nm}$	AA	pure water	2200	N/A	[4]
FS-COF+WS5F	$\lambda > 420 \text{ nm}$	AA	pure water	1300	N/A	[5]
CN/WP@NC	$\lambda > 420 \text{ nm}$	TEOA	NaCl	1217	7.98 (420 nm)	[6]
CZS@S-1	$\lambda > 420 \text{ nm}$	Na <sub>2</sub> S/Na <sub>2</sub> SO <sub>3</sub>	MgCl <sub>2</sub>	42000	N/A	[7]
TiO <sub>2</sub> .ZnS <sub>2</sub>	$\lambda > 420 \text{ nm}$	Na <sub>2</sub> S/Na <sub>2</sub> SO <sub>3</sub>	pure water	5503	N/A	[8]
MoS <sub>2</sub> @TiO <sub>2</sub>	AM 1.5	TEOA	pure water	21600	N/A	[9]
oCND-2	AM 1.5	TEOA	seawater	19700	N/A	[10]
SiO <sub>2</sub> /Ag@TiO <sub>2</sub>	$\lambda > 400 \text{ nm}$	Glycerol	NaCl	800	N/A	[11]
CdxZn <sub>1-x</sub> Se	AM 1.5	Na <sub>2</sub> SO <sub>3</sub> and Na <sub>2</sub> S	seawater	36600	11.8 (520 nm)	[12]
Ti-O-Si (400)	$\lambda > 420 \text{ nm}$	TEOA	NaCl	1640	N/A	[13]
Ti <sub>3</sub> C <sub>2</sub> /Cd <sub>0.5</sub> Zn <sub>0.5</sub> S	$\lambda > 420 \text{ nm}$	Na <sub>2</sub> SO <sub>3</sub> and Na <sub>2</sub> S	seawater	9071	N/A	[14]
WS <sub>2</sub> @C-TiO <sub>2</sub> on g-C <sub>3</sub> N <sub>4</sub>	$\lambda > 420 \text{ nm}$	TEOA	seawater	1199	N/A	[15]
COP-TF@CNi <sub>2</sub> P	$\lambda > 420 \text{ nm}$	Na <sub>2</sub> SO <sub>3</sub> and Na <sub>2</sub> S	seawater	2500	N/A	[16]
UCOF-SCAU-2	$\lambda > 420 \text{ nm}$	AA	pure water	96	6.87 (365 nm)	[17]
ZIS-P200	$\lambda > 400 \text{ nm}$		seawater	92	0.16 (365 nm)	[18]

<sup>a</sup>2 mg COFs,  $\lambda > 420 \text{ nm}$ , 300 mW/cm<sup>2</sup>, 0.1 M ascorbic acid, pH=3.5, room temperature, 5 h.

**Table S10.** Hydrogen evolution performance with co-catalysts

Photocatalyst	Illumination	HEC	SED	Solution	Activity ( $\mu\text{mol g}^{-1} \text{h}^{-1}$ )	AQE (%)	Ref.
TpPaCl	$\lambda > 420 \text{ nm}$	Pt	AA	pure water	137631 <sup>a</sup>	7.54	This work
		Pt	AA	seawater	188122 <sup>b</sup>	(420 nm)	
ZnPor-DETH-COF	$\lambda > 420 \text{ nm}$	Pt	TEOA	pure water	403	0.063 (450 nm)	[2]
BT-COF	$\lambda > 420 \text{ nm}$	Pt	AA	pure water	7700	7.53 (420 nm)	[3]
Py-CITP-BT-COF	$\lambda > 420 \text{ nm}$	Pt	AA	pure water	8875	8.45 (420 nm)	[4]
FS-COF+WS5F	$\lambda > 420 \text{ nm}$	Pt	AA	pure water	16300	3.2 (420 nm)	[5]
COF-JLU100	$\lambda > 420 \text{ nm}$	Pt	TEOA	pure water	107308	5.13 (450 nm)	[19]
PY-DHBD-COF	$\lambda > 420 \text{ nm}$	Pt	AA	pure water	71160	8.4 (450 nm)	[20]
COF-935	$\lambda > 420 \text{ nm}$	Pt	AA	pure water	67550	3.39	[21]
	$\lambda > 420 \text{ nm}$	Pt	AA	seawater	18890	(420 nm)	
TpPa	$\lambda > 420 \text{ nm}$	Pt	AA	seawater	41300	0.57 (420 nm)	[22]
P-8CE	$\lambda > 420 \text{ nm}$	Pt	TEA	seawater	38900	3.39 (420 nm)	[23]
COF-923	$\lambda > 420 \text{ nm}$	Pt	AA	pure water	7824	0.68 (450 nm)	[24]
BUCT-COF-20	$\lambda > 420 \text{ nm}$	Pt	AA	seawater	40360	N/A	[25]
COF-954	$\lambda > 420 \text{ nm}$	Pt	AA	seawater	70410	N/A	[26]
TpPa( $\Delta$ )-Cu(II)-COF	$\lambda > 420 \text{ nm}$	Cu	Cysteine(L)	pure water	14720	0.78 (600 nm)	[27]
Co/Zn-Salen-COF	$\lambda > 420 \text{ nm}$	Co	AA	pure water	1378	0.78 (600 nm)	[28]
Pt-Tpy-COF	$\lambda > 420 \text{ nm}$	Pt	AA	pure water	7800	3.39 (420 nm)	[29]

<sup>a</sup>0.5 mg COFs,  $\lambda > 420 \text{ nm}$ , 300 mW/cm<sup>2</sup>, 0.1 M ascorbic acid, pH=2.8, room temperature, 5 h. <sup>b</sup>0.5 mg COFs,  $\lambda > 420 \text{ nm}$ , 300 mW/cm<sup>2</sup>, 0.1 M ascorbic acid, 2 wt% Pt/TpPaCl, pH=3.5, room temperature, 5 h.

## References

- [1] S. Grimme, S. Ehrlich, L. Goerigk, Effect of the damping function in dispersion corrected density functional theory, *J. Comput. Chem.*, 2011, **32**, 1456-1465.
- [2] R. Chen, Y. Wang, Y. Ma, A. Mal, X.Y. Gao, L. Gao, L. Qiao, X.B. Li, L.Z. Wu, C. Wang, Rational design of isostructural 2D porphyrin-based covalent organic frameworks for tunable photocatalytic hydrogen evolution, *Nat. Commun.*, 2021, **12**, 1354.
- [3] T. Zhou, L. Wang, X. Huang, J. Unruangsri, H. Zhang, R. Wang, Q. Song, Q. Yang, W. Li, C. Wang, K. Takahashi, H. Xu, J. Guo, PEG-stabilized coaxial stacking of two-dimensional covalent organic frameworks for enhanced photocatalytic hydrogen evolution, *Nat. Commun.*, 2021, **12**, 3934.
- [4] W. Chen, L. Wang, D. Mo, F. He, Z. Wen, X. Wu, H. Xu, L. Chen, Modulating Benzothiadiazole-Based Covalent Organic Frameworks via Halogenation for Enhanced Photocatalytic Water Splitting, *Angew. Chem. Int. Ed.*, 2020, **59**, 16902-16909.
- [5] X. Wang, L. Chen, S.Y. Chong, M.A. Little, Y. Wu, W.H. Zhu, R. Clowes, Y. Yan, M.A. Zwijnenburg, R.S. Sprick, A.I. Cooper, Sulfone-containing covalent organic frameworks for photocatalytic hydrogen evolution from water, *Nat. Chem.*, 2018, **10**, 1180-1189.
- [6] T. Song, X. Zhang, K. Matras-Postolek, P. Yang, N-doped carbon layer promoted charge separation/transfer in WP/g-C<sub>3</sub>N<sub>4</sub> heterostructures for efficient H<sub>2</sub> evolution and 4-nitrophenol removal, *Carbon*, 2023, **202**, 378-388.
- [7] Y. Yuan, F.-J. Wu, S.-T. Xiao, Y.-T. Wang, Z.-W. Yin, G. Van Tendeloo, G.-G. Chang, G. Tian, Z.-Y. Hu, S.-M. Wu, X.-Y. Yang, Hierarchical zeolites containing embedded Cd<sub>0.2</sub>Zn<sub>0.8</sub>S as a photocatalyst for hydrogen production from seawater, *Chem. Commun.*, 2023, **59**, 7275-7278.
- [8] Q. Wang, G. Wang, J. Wang, J. Li, K. Wang, S. Zhou, Y. Su, In Situ Hydrothermal Synthesis of ZnS/TiO<sub>2</sub> Nanofibers S-Scheme Heterojunction for Enhanced Photocatalytic H<sub>2</sub> Evolution, *Adv. Sustainable Syst.*, 2023, **7**, 2200027.
- [9] X. Hu, S. Lu, J. Tian, N. Wei, X. Song, X. Wang, H. Cui, The selective deposition of MoS<sub>2</sub> nanosheets onto (101) facets of TiO<sub>2</sub> nanosheets with exposed (001) facets and their enhanced photocatalytic H<sub>2</sub> production, *Appl. Catal., B*, 2019, **241**, 329-337.
- [10] B. Jana, Y. Reva, T. Scharl, V. Strauss, A. Cadanel, D.M. Guldi, Carbon Nanodots for All-in-One Photocatalytic Hydrogen Generation, *J. Am. Chem. Soc.*, 2021, **143**, 20122-20132.
- [11] M. Gao, P.K.N. Connor, G.W. Ho, Plasmonic photothermic directed broadband sunlight harnessing for seawater catalysis and desalination, *Energy Environ. Sci.*, 2016, **9**, 3151-3160.
- [12] B. Qiu, Q. Zhu, M. Xing, J. Zhang, A robust and efficient catalyst of Cd<sub>x</sub>Zn<sub>1-x</sub>Se motivated by CoP for photocatalytic hydrogen evolution under sunlight irradiation, *Chem. Commun.*, 2017, **53**, 897-900.
- [13] T. Song, P. Zhang, T. Wang, A. Ali, H. Zeng, Constructing a novel strategy for controllable synthesis of corrosion resistant Ti<sup>3+</sup> self-doped titanium–silicon materials with efficient hydrogen evolution activity from simulated seawater, *Nanoscale*, 2018, **10**, 2275-2284.
- [14] G. Zeng, Y. Cao, Y. Wu, H. Yuan, B. Zhang, Y. Wang, H. Zeng, S. Huang, Cd<sub>0.5</sub>Zn<sub>0.5</sub>S/Ti<sub>3</sub>C<sub>2</sub> MXene as a Schottky catalyst for highly efficient photocatalytic hydrogen evolution in seawater, *Appl. Mater. Today*, 2021, **22**, 100926.
- [15] C. Yang, J. Qin, S. Rajendran, X. Zhang, R. Liu, WS<sub>2</sub> and C-TiO<sub>2</sub> Nanorods Acting as Effective Charge Separators on g-C<sub>3</sub>N<sub>4</sub> to Boost Visible-Light Activated Hydrogen Production from Seawater, *ChemSusChem*, 2018, **11**, 4077-4085.
- [16] Y. Liu, Z. Xiang, Fully Conjugated Covalent Organic Polymer with Carbon-Encapsulated Ni<sub>2</sub>P for Highly Sustained Photocatalytic H<sub>2</sub> Production from Seawater, *ACS Appl. Mater. Interfaces*, 2019, **11**, 41313-41320.
- [17] R. Shen, C. Qin, L. Hao, X. Li, P. Zhang, X. Li, Realizing Photocatalytic Overall Water Splitting by Modulating the Thickness-Induced Reaction Energy Barrier of Fluorenone-Based Covalent Organic Frameworks, *Adv. Mater.*, 2023, **35**, 2305397.
- [18] B.-J. Ng, W.-K. Chong, L.K. Putri, X.Y. Kong, J. Low, H.W. Lee, L.-L. Tan, W.S. Chang, S.-P. Chai, Heteroatom

- P filling activates intrinsic S atomic sites of few-layered ZnIn<sub>2</sub>S<sub>4</sub> via modulation of H adsorption kinetics for sacrificial agent-free photocatalytic hydrogen evolution from pure water and seawater, *J. Mater. Chem. A*, 2023, **11**, 17079-17090.
- [19] S. Ma, T. Deng, Z. Li, Z. Zhang, J. Jia, Q. Li, G. Wu, H. Xia, S.W. Yang, X. Liu, Photocatalytic Hydrogen Production on a sp<sup>2</sup>-Carbon-Linked Covalent Organic Framework, *Angew. Chem. Int. Ed.*, 2022, **61**, e202208919.
- [20] Y. Li, L. Yang, H. He, L. Sun, H. Wang, X. Fang, Y. Zhao, D. Zheng, Y. Qi, Z. Li, W. Deng, In situ photodeposition of platinum clusters on a covalent organic framework for photocatalytic hydrogen production, *Nat. Commun.*, 2022, **13**, 1355.
- [21] K. Wang, Y. Zhong, W. Dong, Y. Xiao, S. Ren, L. Li, Intermediate Formation of Macrocycles for Efficient Crystallization of 2D Covalent Organic Frameworks with Enhanced Photocatalytic Hydrogen Evolution, *Angew. Chem. Int. Ed.*, 2023, **62**, e202304611.
- [22] Q. Yue, G. Li, P. Fu, B. Meng, F. Ma, Y. Zhou, J. Wang, In-situ polarization of covalent organic frameworks in seawater enables enhanced photocatalytic hydrogen evolution under visible-light irradiation, *Nano Research*, 2023, **16**, 6251-6259.
- [23] C.L. Chang, T.F. Huang, W.C. Lin, L.Y. Ting, C.H. Shih, Y.H. Chen, J.J. Liu, Y.T. Lin, Y.T. Tseng, Y.H. Wu, Y.E. Sun, M.H. Elsayed, C.W. Chen, C.H. Yu, H.H. Chou, Synergistic Effect of Crown Ether and Main-Chain Engineering for Boosting Hydrogen Evolution of Polymer Photocatalysts in Seawater, *Adv. Energy Mater.*, 2023, **13**, 2300986.
- [24] W. Dong, Z. Qin, K. Wang, Y. Xiao, X. Liu, S. Ren, L. Li, Isomeric Oligo(Phenylenevinylene)-Based Covalent Organic Frameworks with Different Orientation of Imine Bonds and Distinct Photocatalytic Activities, *Angew. Chem. Int. Ed.*, 2022, **62**, e202216073.
- [25] Y. Wang, Z. Qiao, H. Li, R. Zhang, Z. Xiang, D. Cao, S. Wang, Molecular Engineering for Modulating Photocatalytic Hydrogen Evolution of Fully Conjugated 3D Covalent Organic Frameworks, *Angew. Chem. Int. Ed.*, 2024, **63**, e202404726.
- [26] Y. Zhong, W. Dong, S. Ren, L. Li, Oligo(phenylenevinylene)-Based Covalent Organic Frameworks with Kagome Lattice for Boosting Photocatalytic Hydrogen Evolution, *Adv. Mater.*, 2023, **36**, 2308251.
- [27] W. Weng, J. Guo, The effect of enantioselective chiral covalent organic frameworks and cysteine sacrificial donors on photocatalytic hydrogen evolution, *Nat. Commun.*, 2022, **13**, 5768.
- [28] W. Zhou, Q.W. Deng, H.J. He, L. Yang, T.Y. Liu, X. Wang, D.Y. Zheng, Z.B. Dai, L. Sun, C. Liu, H. Wu, Z. Li, W.Q. Deng, Heterogenization of Salen Metal Molecular Catalysts in Covalent Organic Frameworks for Photocatalytic Hydrogen Evolution, *Angew. Chem. Int. Ed.*, 2022, **62**, e202214143.
- [29] C. Liu, D.-L. Ma, P.-J. Tian, C. Jia, Q.-Y. Qi, G.-F. Jiang, X. Zhao, Lateral functionalization of a one-dimensional covalent organic framework for efficient photocatalytic hydrogen evolution from water, *J. Mater. Chem. A*, 2024, **12**, 16063-16069.